

1 **Basalt, Unveiling Fluid-filled Fractures, Inducing Sediment Intra-void Transport, Ephemeraly:**
2 examples from Katla 1918

3 Jacqueline Owen^{a*}, Thomas Shea^b, Hugh Tuffen^a

4 ^aLancaster Environment Centre, Lancaster University, Lancaster, LA1 4YQ. UK

5 ^bDepartment of Geology and Geophysics, SOEST, University of Hawaii, Honolulu, HI, 96822. USA

6 [*j.owen2@lancaster.ac.uk](mailto:j.owen2@lancaster.ac.uk)

7 Abstract

8 This article documents textures within Katla 1918 pyroclasts, where particle-filled fractures and
9 bubbles have been observed. These features are analogous to tuffisite veins; particle-filled fractures
10 which represent the preserved remains of transient degassing pathways in shallow conduits.

11 Such fractures have long been considered restricted to high viscosity silicic melts. However, through
12 BSE images and compositional maps, we have identified similar tuffisite-like features in crystal-poor
13 basalt pyroclasts from the 1918 A.D. subglacial eruption of Katla, Iceland (K1918). Clast textures record
14 transient mobility of juvenile/lithic particles, melt droplets and gas through magmatic fractures and
15 connected vesicles. Key evidence includes (1) the presence of variably sintered fine-ash particles
16 within variably healed fractures and vesicles (present in >80% of clasts analysed), (2) compositional
17 maps that reveal the presence of foreign particles within preserved and healed permeable pathways,
18 and (3) lower vesicularities immediately surrounding 'fracture' walls, suggestive of diffusive volatile
19 loss into a permeable network.

20 The 1918 A.D. eruption of Katla occurred under a thick glacier, however the ice was quickly breached,
21 owing partly to the explosive nature of the eruption. We propose that the formation and preservation
22 of these transient permeable networks have been facilitated by rapid decompression of a relatively
23 volatile-rich magma, in a confined subglacial environment, with combined magmatic and
24 phreatomagmatic fragmentation, followed by rapid quenching by meltwater.

25 Tuffisite veins in rhyolite demonstrate repeated fracture-healing cycles, which drive incremental
26 release of overpressured gas and help to defuse explosive eruptions. Interestingly, the permeable
27 network at Katla failed to defuse the 1918 A.D. eruption, which involved a particularly violent
28 subglacial eruptive phase. It is unclear whether this demonstrates an inability of mafic tuffisite-like
29 features to efficiently degas magma (perhaps owing to the especially transient nature of permeable
30 pathways in low viscosity magmas) or an ability to enhance fragmentation by providing infiltration
31 pathways for external water. The latter scenario may explain the rapid melting of the overlying glacier
32 as the large surface area-to-volume ratio of fractured magma would allow rapid heat transfer.

33 Nevertheless, we document a previously undescribed texture in basaltic magmas. It is intriguing why
34 it has not, to the best of our knowledge, been documented elsewhere. Have these permeable
35 pathways been over-looked in the past (e.g. mistaken for bad sample preparation or not noticed
36 without high magnification BSE images) and are in fact a widespread phenomenon in subglacial (and
37 other?) basalts; or do our samples in fact represent a rarely preserved texture? Either way, they offer
38 a new insight into the degassing and fragmentation of subglacial basalt.

39

40 Keywords: degassing; vesicles; open-system degassing; phreatomagmatic; tuffisite veins; Katla

41

42 Introduction

43 Due to the ability of volcanic gases to rapidly expand at low pressure, volatiles are often considered
44 the driving force for explosive volcanism (Sparks, 1978; Moore et al., 1998; Blundy et al., 2006), with
45 violent fragmentation typically fuelled by high volatile contents and closed system degassing (i.e.
46 where the volatiles remain trapped within the magma) (Anderson and Fink, 1989; Hoblitt and Harmon,
47 1993; Anderson et al., 1995; Martel et al., 1998; Villemant and Boudon, 1998; Villemant and Boudon,
48 1999; Villemant et al., 2003; Adams et al., 2006; Villemant et al., 2008; Humphreys et al., 2009; Owen
49 et al., 2013a). Transitions to effusive volcanism are often characterized by a shift towards open system
50 degassing behaviour, where volatiles are able to efficiently outgas from the magma (Jaupart and
51 Allègre, 1991; Jaupart, 1998; Namiki and Manga, 2008; Owen et al., 2013b).

52 Magma outgassing occurs according to different mechanisms that strongly depend on melt
53 composition (Vergnolle and Jaupart, 1986; Houghton and Gonnermann, 2008). The low viscosity of
54 basalt, coupled with high volatile diffusivities in basaltic melts, enables bubbles to rapidly grow and
55 buoyantly rise through the magma column, allowing efficient magma-gas separation and open-system
56 degassing (Wilson, 1980; Vergnolle and Jaupart, 1986; Edmonds and Gerlach, 2007; Menand and
57 Phillips, 2007; Houghton and Gonnermann, 2008). In contrast, the high viscosity and lower volatile
58 diffusivities in silicic melts hinder both bubble growth (Proussevitch and Sahagian, 1996) and melt-
59 bubble decoupling (Sparks, 1978). However, high-Si magmas can still experience open system
60 degassing by becoming permeable, either with connected bubbles acting as a pathway for gas to flow
61 (Eichelberger et al., 1986; Westrich and Eichelberger, 1994; Klug and Cashman, 1996; Namiki and
62 Manga, 2008), and/or by the creation of tuffisite veins, permeable gas and ash filled fracture networks
63 that temporarily exist within the magma conduit (Sparks, 1997; Tuffen et al., 2003; Saubin et al., 2016;
64 Farquharson et al., 2017).

65 Magma fracturing and tuffisite vein formation are currently thought to be limited to high viscosity
66 magmas such as rhyolites (Tuffen et al., 2003; Castro et al., 2012; Saubin et al., 2016), crystal-rich
67 andesites (Kolzenburg et al., 2012; Plail et al., 2014; Kendrick et al., 2016) and dacites (Nakada et al.,
68 2005; Noguchi et al., 2008; Gaunt et al., 2014). Tuffisite veins within conduits, are proposed to form
69 when highly viscous magma experiences failure either due to gas overpressure or shear fracture within
70 the glass transition (T_g) interval. These fractures then act as a pathway for gas and fragmented
71 particles that eventually obstruct the vein. Subsequent welding of these particles results in vein
72 healing and permeable pathway occlusion, leading to re-pressurisation (Tuffen et al., 2003). Slow
73 crystallisation rates in rhyolite allow prolonged magma residence in the glass transition interval (hours
74 or days), providing sufficient time for repeated fracture-healing episodes within crystal-poor melt, and
75 creating superimposed generations of tuffisite veins within flow-banded glass (Tuffen et al., 2003;
76 Gonnermann and Manga, 2005).

77 In contrast, the low viscosity of basalt means that repeated episodes of fracturing and healing within
78 the conduit are unlikely. Inherently, it is much harder to fragment/fracture basaltic magma at eruptive

79 temperatures (Papale, 1999; Giordano and Dingwell, 2003) without decreasing temperature,
80 increasing crystallinity (Giordano and Dingwell, 2003; Houghton and Gonnermann, 2008; Namiki and
81 Manga, 2008) and/or by invoking rapid decompression and/or magma-water interaction (Giordano
82 and Dingwell, 2003). These processes will all hinder subsequent sintering, as rapid cooling would serve
83 to quench the magma and high crystallinities lower the available melt fraction. Therefore, even if
84 fracturing were able to occur in a crystal-free basaltic melt, rapid crystallisation will limit its residence
85 time in the T_g interval, allowing little time for sintering, vein healing or repeated fragmentation cycles
86 (Tuffen et al., 2003). It is perhaps not surprising that, to our knowledge, there is no documented
87 evidence of tuffsite-like features within basaltic magma.

88 In this paper we present some of the first observations supporting transient particle transport and
89 sintering within permeable pathways (fractures, connected vesicles and inter-clast void spaces) in a
90 high-temperature, crystal-poor basalt. This process likely preceded powerful hydromagmatic
91 fragmentation, emphasising a need to better understand the influence of open-system degassing and
92 clast recycling in basaltic eruptions.

93 2. Materials and methods

94 2.1 Geological background and sampling

95 Samples were collected within deposits from the 1918 A.D. VEI 4 (Smithsonian, 2016) subglacial
96 basaltic eruption of Katla (K1918) in South Iceland (Fig. 1a). The eruption took just two hours to melt
97 through ~400 m of overlying ice (Mýrdalsjökull glacier), after which both an ash plume and a
98 jökulhlaup (glacial flood) were observed (Tómasson, 1996; Sturkell et al., 2010). The plume was 14 km
99 high, and deposited ash over 50,000 km² of land (Larsen, 2010). The jökulhlaup transported 0.7-1.6
100 km³ of tephra (Larsen, 2000), with an inferred peak discharge rate of >300,000 m³ s⁻¹ (Tómasson,
101 1996), making it the 14th most powerful flood of the Quaternary (last 2.6 million years) (O'Connor and
102 Costa, 2004). Both the jökulhlaup and the extreme melting rate of the glacier were exceptional and
103 cannot be readily explained by existing models of convective magma-ice heat transfer (Gudmundsson
104 et al., 1997; Hoskuldsson and Sparks, 1997; Wilson and Head, 2002; Gudmundsson, 2013; Woodcock
105 et al., 2014; Woodcock et al., 2015; Woodcock et al., 2016).

106 Samples characterised in this study were collected from both the air-fall and the jökulhlaup deposit.
107 Wind blew ash from the eruption plume in many directions but predominantly to the NE (Larsen, 2010;
108 Larsen et al., 2014), with ~300 g m⁻² reaching North Iceland (Larsen et al., 2014). However, the ash was
109 poorly preserved following the eruption. Nevertheless, K1918 ash can be found in select soil horizons
110 around Katla (Óladóttir et al., 2005; Óladóttir et al., 2008), and the thickest deposit is observed as a
111 layer in the Mýrdalsjökull ice, which is now being exhumed (Gudmundsson, 2013, pers. comm).

112 The K1918 jökulhlaup deposit has been well characterised by a variety of studies (e.g. Maizels, 1992;
113 Maizels, 1993; Tómasson, 1996; Duller et al., 2008; Russell et al., 2010). Maizels (1992) identified four
114 units; 1: a basal unit of massive gravels and imbricated clast-supported gravels that represents rising
115 flow, overlain by 2: massive pumice granules interpreted to be part of a flow surge, overlain by 3:
116 trough cross-bedded pumice granules, and finally 4: horizontally bedded pumice granules and pumice
117 sands, with the top two units representing more fluid waning stages of the jökulhlaup. The deposit is
118 ~12 m thick in proximal regions, decreasing to 4 m thick at the coast, some 18 km away (Maizels,
119 1992).

120 Air-fall tephra was collected from Sólheimajökull glacier (Fig. 1a) where a ~40-cm thick layer of
121 typically sub-cm clasts are preserved in the ice (Fig. 1b). These samples are prefixed "Sol". Jökulhlaup
122 samples (prefixed "Mul") were collected from the banks of the Múlakvísl river, where river
123 downcutting has exposed a clear vertical cross-section through the deposit (Fig. 1c). In both settings
124 multiple locations were sampled, which is denoted by the second part of the sample name. At
125 Múlakvísl we focussed on a 3 m high exposure (Figs. 1a, 1c). In both locations, there were multiple
126 layers, each of which was sampled. The layer makes up the third part of the sample name. For the air-
127 fall tephra six layers were documented and labelled A-F (Fig. 1b). The observed stratigraphy at the
128 jökulhlaup deposit matches the units described in Maizels (1992), Duller et al. (2008) and Russell et al.
129 (2010) but with only units 2-4 exposed (Fig. 1c). The lower and upper half of unit 3 appeared more
130 lithic- and juvenile-rich respectively and was separated by a vein. As a result, we collected two samples
131 from unit 3 and labelled them 3a and 3b respectively (Fig. 1c).

132 Grain size distributions revealed that for the samples collected, the largest clast sizes typically fell
133 within the -3 to -4 ϕ category (8-16 mm) and had a peak at the -1 to -2 ϕ category (2-4 mm). Typical
134 air fall samples had a second modal group with a high proportion < 125 μm (>3 ϕ). However, it should
135 be noted that, in both settings, the grain size distribution is probably a reflection of the transportation,
136 and potentially the re-mobilisation, history and not thought to represent the true volcanic deposition.
137 This is especially true of the jökulhlaup deposit where it is thought that the majority of the fines and
138 most of the early material was washed out to sea (Duller et al., 2008). Nevertheless, for each key
139 sample, four representative 8-16 mm and nine 2-4 mm clasts were chosen, numbered and made into
140 thin sections. The clast size and number make up the fourth and fifth (final) parts of the sample name,
141 respectively. In total 100 clasts of this size were thin sectioned and of these, 26 representative clasts
142 (9 air-fall and 17 jökulhlaup samples) were chosen for backscatter imaging. Thin sections were also
143 made of the 250-500 μm clast size to supplement the geochemistry data.

144 Each sample name, therefore, has the following format 1) environmental setting 2) location number,
145 3) layer/unit reference, 4) clast size, 5) clast number.

146



147

148 Figure 1: (a) Map of the Katla area showing the sampling locations with the inlet showing the
 149 position in South Iceland; (b) Cross-section through the air-fall deposit on Sólheimajökull glacier
 150 showing units A-F; (c) Cross-section of the jökulhlaup deposit at Múlakvísl showing the different
 151 units sampled (units 2 to 4 from Duller et al. (2008)) with a meter rule for scale.

152 2.2 Geochemistry and imaging (EPMA)

153 A Field-emission JEOL Hyperprobe JXA-8500F Electron Probe Micro-Analyser (EPMA) at the
 154 University of Hawaii was used to acquire (a) back-scattered electron (BSE) images, (b) compositional
 155 (X-ray distribution) maps and (c) spot analyses. Accelerating voltages of 15, 20 and 20 keV and beam
 156 currents of 10, 30-50, and 10 nA were used for (a), (b) and (c) respectively. Spot sizes of 1 μm , 2 μm

157 and 10 μm were used for Fe-Ti oxides, K-rich particles and matrix glass, respectively. On-peak count
158 times of 30 s were used for Si, Al, Fe, Mn, Na, K, P, and 65-70 s for Al, Mg, Ca, and Cl. Time-dependent
159 intensity corrections were used for glass analyses when significant Na loss or Si gains were detected
160 (e.g. Shea et al., 2014).

161 To assess compositional heterogeneity and relative element abundances in select samples,
162 compositional maps of Fe, Ca and K were obtained using three of the five spectrometers and dwell
163 times of 40-45 msec/pixel. Raw data was used to make single 2D intensity matrices, which were then
164 combined as individual channels into a single RGB composite image. The other two spectrometers
165 measured S and either F or Na. Intensity matrices for all measured elements are provided in Appendix
166 1 (Figs. A1-A3).

167 Spot analyses were mainly performed on magnetite and ilmenite crystals for geothermometry (see
168 section 2.3). A limited number of glass analyses were also acquired and compared to EPMA data
169 collected from the University of Edinburgh. There, > 200 glass measurements were made on more
170 than 50 different air-fall and jökulhlaup clasts. All analyses were carried out at 15 kV with a 5 μm spot
171 size. Beam currents of 2 and 80 nA were used for major and minor/trace elements respectively as per
172 Hayward (2011). Analyses with totals < 97 wt.% and those with a clear influence of crystals were
173 rejected.

174 2.3 Estimating eruption temperature (geothermometry)

175 To better constrain the physical parameters of the melt (e.g. viscosity, diffusion rates, sintering rates
176 etc.) oxide geothermometry was used to estimate the magma eruptive temperature. Using the
177 method described in section 2.2, 61 measurements were made of magnetite and ilmenite crystals
178 within both jökulhlaup and air-fall samples. These were converted into temperatures using the Fe-Ti
179 oxide geothermobarometer model of Ghiorso and Evans (2008). Measurements were rejected if either
180 SiO_2 exceeded 1 wt.%, as this may reflect mixed analyses with surrounding glass, or if they failed the
181 equilibrium test of Bacon and Hirschmann (1988).

182 2.4 Glass H_2O content (FTIR)

183 The glass water contents of five clasts (one air-fall and four jökulhlaup) were measured using Fourier
184 Transform Infrared Spectroscopy (FTIR). A Thermo Nicolet IR interferometer, with KBr beamsplitter,
185 Continuum Analytical microscope and MCT-A detector were used at Lancaster University. Each
186 measurement (including background analyses) constituted 256 spectra collected at 4 cm^{-1} resolution
187 over the range 600-5500 cm^{-1} . A minimum of ten measurements were taken per sample with a
188 100x100 μm aperture.

189 H_2O contents (C) were determined using the Beer-Lambert law (e.g. Stolper, 1982)

$$190 \quad C = \frac{M_w A}{d \rho \epsilon}$$

191 (1)

192 where M_w is the molecular weight of water (18.02 g mol^{-1}), A is peak height, d is sample thickness (in
193 cm), ρ is density (2,770 g l^{-1} estimated using the density calculator of Bottinga and Weill (1970) and a

194 representative composition of K1918 basalt taken from Óladóttir et al. (2008)), and ϵ is the absorption
195 coefficient ($\text{l mol}^{-1} \text{cm}^{-1}$).

196 Total H_2O (H_2O_i) concentrations were determined using the absorption peak at 3550 cm^{-1} and an
197 absorption coefficient of $63 \text{ l mol}^{-1} \text{cm}^{-1}$ (Dixon et al., 1988). Sample thickness was determined using a
198 Mitutoyo digital displacement gauge accurate to $\pm 3 \mu\text{m}$.

199 The characteristic double CO_3^{2-} peaks (1515 and 1435 cm^{-1}) and the molecular H_2O (H_2O_m) peak at
200 1630 cm^{-1} were indiscernible, suggestive of very low CO_2 and H_2O_m concentrations. As post quenching
201 hydration favours H_2O_m (Yokoyama et al., 2008; Denton et al., 2009), it is unlikely that our K1918
202 samples have undergone this process.

203

204 3 Results

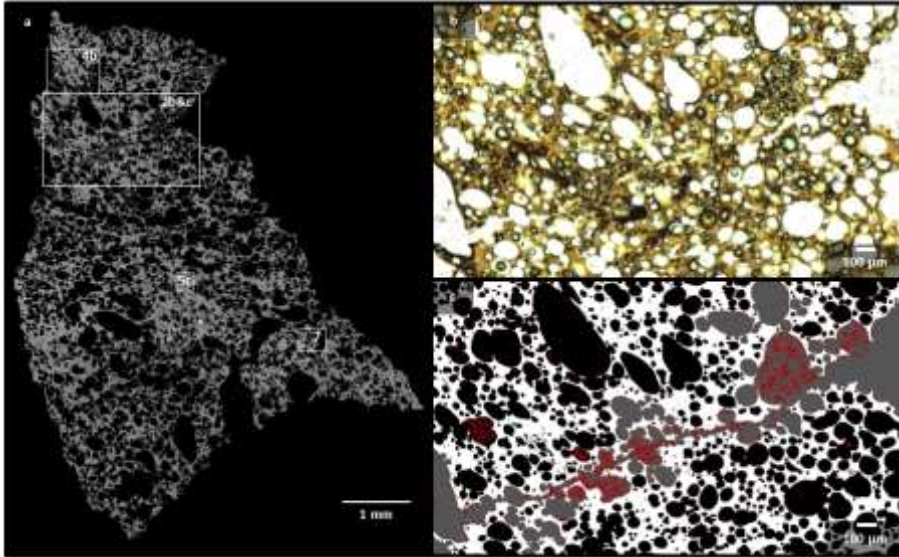
205 3.1 Overview of clasts

206 Clasts tend to be brown, black (or a mixture of the two) and contain sparse phenocrysts. The brown
207 material (e.g. Figs. 2b, 3, 4bii) is clear glass (sideromelane), with few microlites (typically 5-25% for air-
208 fall and $< 5\%$ for jökulhlaup clasts), in contrast to the black (tachylite) material (e.g. Fig. 4aii), which is
209 relatively microlite-rich (~ 30 -70%), opaque and contains bubbles that are largely obscured in plane-
210 polarised light (ppl) microscopy. Air-fall clasts are typically 40-50% vesicular whilst jökulhlaup clasts
211 are ~ 60 -75% vesicular, with a large number of small bubbles (Owen et al., 2017). Bubble and microlite
212 textures are often locally heterogeneous throughout each clast. The clasts often contain fractures,
213 connected bubbles and textural evidence of sintering, which are particularly well preserved in the
214 jökulhlaup samples (see sections below). Note that in this paper, we will use the term 'sintering' in
215 reference to a texture that shows any of the stages of sintering from contact point fusing, to full
216 coalescence into a solid mass. In addition to the brown and black clasts, there is a small percentage of
217 pale/clear lithic clasts that are largely void of both phenocrysts and vesicles.

218 3.2 Fractures

219 Most clasts contain fractures that have either a ragged, sharp angular appearance (Fig. 2) or a
220 smoother, more rounded morphology (Fig. 3). Fractures observed are typically millimetric in length
221 and tens to hundreds of μm wide, however observations were limited by clast size ($< 16 \text{ mm}$). It is
222 common for the fractures to be partially filled by ash particles. Ash also occurs within neighbouring
223 vesicles connected to the fractures, but tends to be absent from nearby isolated bubbles (e.g. Fig. 2c).
224 The fracture- and vesicle-occupying particles shall herein be referred to as 'particles', and the host as
225 'clast' to avoid confusion. The fracture-hosted particles are typically of μm scale but can reach $250 \mu\text{m}$
226 in the largest fractures. They are predominantly composed of vesicle-free basalt (both sideromelane
227 and tachylite), but lithics are also present, and some of the larger particles can contain vesicles. The
228 particles tend to be either angular or well rounded, and sometimes appear welded to nearby surfaces
229 (Figs. 4, 5a).

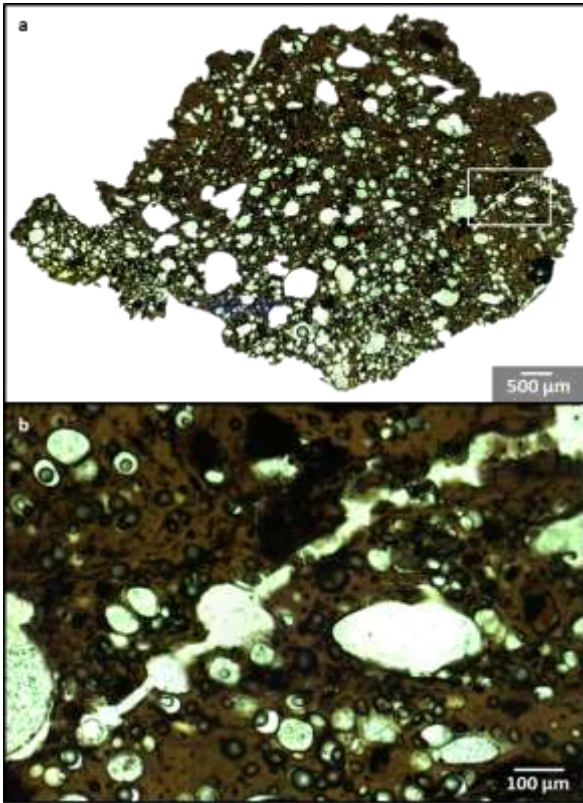
230



231

232 Figure 2: Images showing an angular fracture containing ash particles within sideromelane. (a) A BSE
 233 mosaic image showing the whole clast - jökulhlaup sample Mul 6 unit 3a-1 8,000-16,000 2a (~5x8 mm).
 234 Rectangles with solid lines highlight the area shown in parts b and c, whilst the dashed line rectangles
 235 outline areas shown in Figures 4b, 5c and 7. Figure 8 features within the area shown by Figure 5c but
 236 is too small to depict here; (b) Photomicrograph in ppl detailing the fracture; (c) Simplified BSE image
 237 showing the same area as b, where bubbles have been coloured black, glass white, the background
 238 (and bubbles connected to the background) grey, and ash particles in red.

239

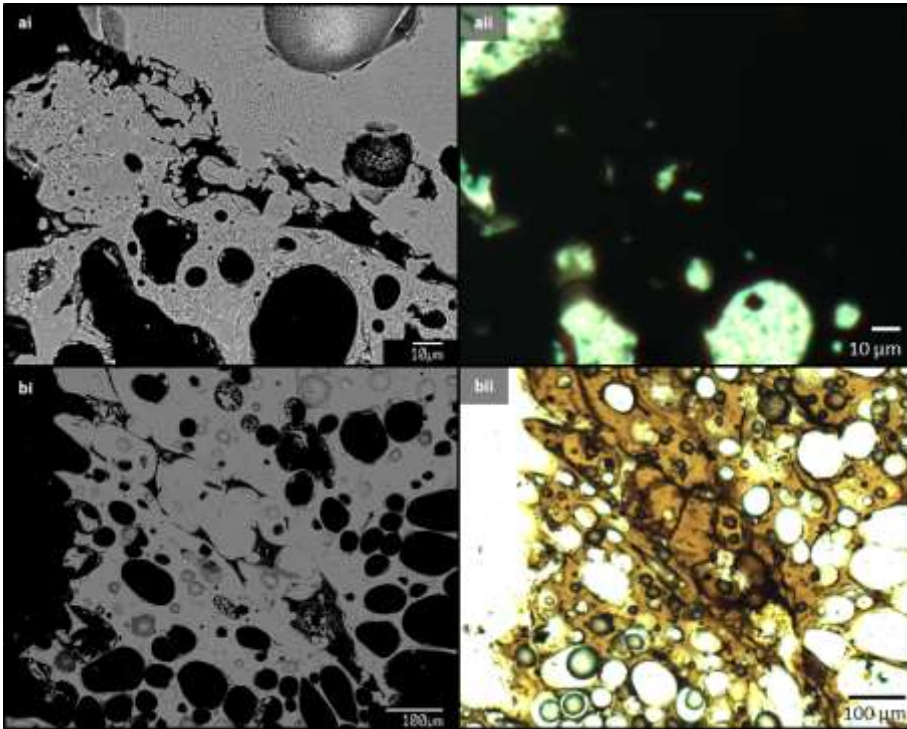


240

241 Figure 3: Photomicrographs in ppl showing a rounded fracture within sideromelane, which contains
242 ash particles near the clast margin. (a) mosaic overview of the whole clast – jökulhlaup sample Mul 6
243 unit 4-1 8,000-16,000 4a (~6x9mm); (b) detail of the fracture, showing a transition from angular (left)
244 to rounded (right) as it approaches the clast margin (far right). The rounded part of the fracture
245 contains ash particles.

246

247



248

249 Figure 4: Images of fractures containing partially sintered particles. The ash particles are connected
 250 to the host, and each other, via 'necks' of various sizes. The suffix refers to the image type, with (i)
 251 denoting BSE images and (ii) denoting thin section images taken in ppl. (a) A ~20 μm wide partially
 252 filled fracture within the tachylite part of a jökulhlaup clast - Mul 6 unit 4-1 8,000-16,000 3a (see
 253 Figure 10a for context). Rounded tachylite ash particles have sintered onto the fracture wall with the
 254 boundary marked by a microlite chain; (b) A ~100 μm wide fracture that has almost healed within a
 255 sideromelane jökulhlaup clast - Mul 6 unit 3a-1 8,000-16,000 2a (see Figure 2a for image location).
 256 The fracture is filled with rounded particles, which have sintered to each other and the fracture
 257 walls. The area immediately adjacent to the fracture is less vesicular than the surrounding melt.

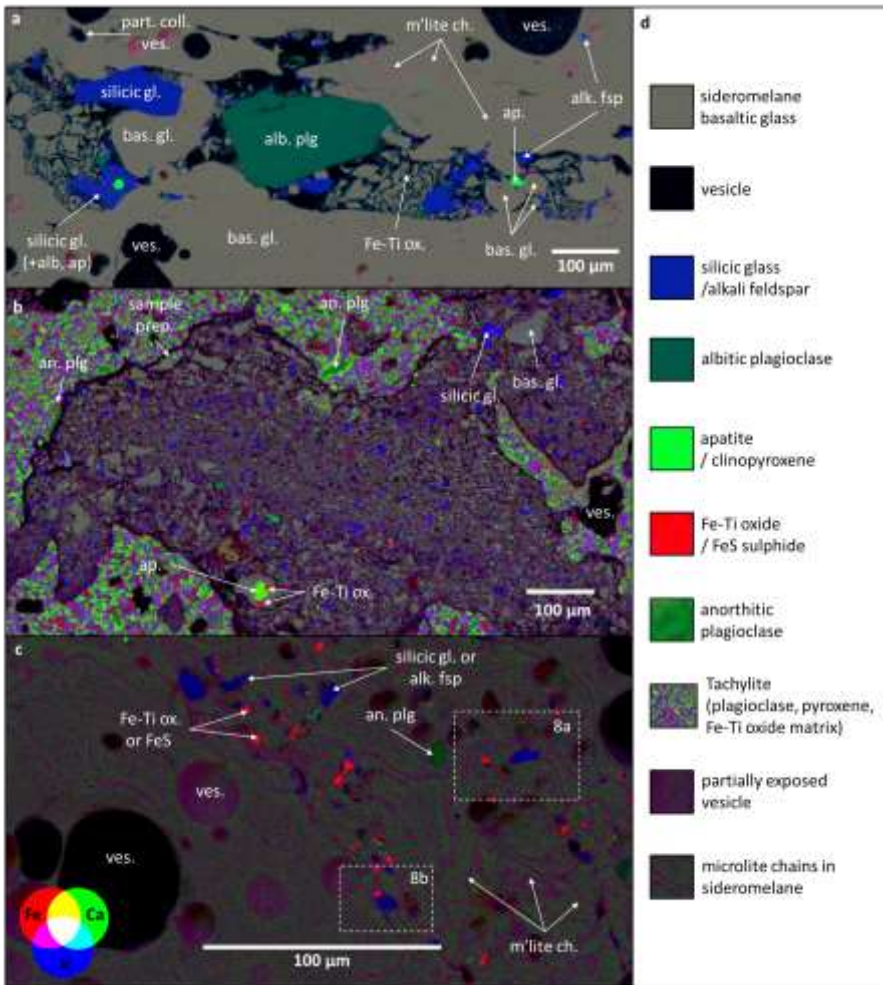
258 As can be seen in Figure 4, the particle-filled fractures, which are fairly evident in the BSE images on
 259 the left, are not at all clear in the ppl images on the right. This is especially true for the tachylite
 260 sample (Fig. 4a) where the opaqueness of the matrix makes the feature (and many of the bubbles)
 261 invisible in ppl (Fig. 4a_{ii}). This is not only true for particle filled fractures but also particle filled
 262 bubbles and in fact most examples of sintering.

263 Particles within fractures and bubbles are noticeably vesicle-poor compared to their host clasts, likely
 264 reflecting their grain size being smaller than the predominant bubble size (Fig. 4a_i). Most particles are
 265 in fact void of vesicles. There are, however, some exceptions, for example the larger fracture-filling
 266 particles in Figure 4b share similar bubble contents and textures to the melt immediately surrounding

267 the fracture. In turn, this area is less vesicular, with typically smaller and less abundant bubbles than
268 material >100 μm away.

269 Compositional mapping of a particle-filled fracture (Fig. 5a) shows that most particles have
270 compositions similar to the surrounding microlite-free host basaltic melt (sideromelane). However,
271 the fracture also contains a significant percentage of K-rich (blue) particles (Fig. 5a), which are mostly
272 also Na-rich, although some are Na-poor (Appendix 1; Fig. A1). There is also a large Na-rich phenocryst
273 (dark green in Fig. 5a) and microlites of this composition within some of the K-rich particles. These
274 K/Na-rich particles likely represent fragments of silicic glass, alkali feldspar, and albitic plagioclase
275 from a more evolved magma. Particles are predominantly sub-angular, but a significant proportion,
276 especially of sideromelane, display rounded morphologies. Some rounded sideromelane particles
277 have viscously deformed around K-rich particles, whilst others are sintered to the fracture walls, with
278 the former boundaries expressed by oxide microlite chains (pink in Fig. 5a). Additional microlite chains
279 occur in the basaltic glass surrounding the fracture, outlining domains that are similar in size and shape
280 to the particles within the fracture. These microlite chains are S-enriched (Fig. A1). Also present in the
281 surrounding glass are a few additional K-rich fragments and partially collapsed vesicles.

282



283

284

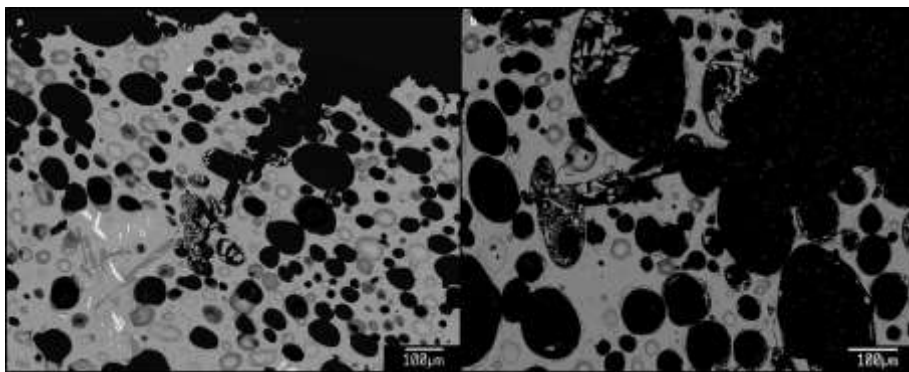
285 Figure 5: Compositional maps showing a particle-filled fracture (a), a particle-filled bubble (b), and a
 286 area of extensive particle-bearing microlite chains (c). Colours represent relative element abundances
 287 according to the legend in the bottom left corner (Fe-rich=red, Ca-rich=green, K-rich=blue, Fe and Ca
 288 -rich=yellow, Ca and K -rich=turquoise, K and Fe -rich=pink and areas rich in Fe, Ca and K=white). (d)
 289 offers an interpretative summary. (a) A ~200 μm wide particle filled fracture within a sideromelane
 290 jökulhlaup clast - Mul 6 unit 3a-1 2,000-4,000 3a. The particles are both basaltic sideromelane and
 291 fragments from a more evolved melt, and have both sub-angular and rounded morphologies. Microlite
 292 chains are present in the surrounding basaltic glass. See Figure 16 for fracture location and ppl/BSE
 293 images; (b) A particle-filled irregularly shaped bubble which appears to be connected to other particle-
 294 filled bubbles (e.g. upper right). The host is microlite-rich tachylite from an air-fall clast - Sol 3E 8,000-
 295 16,000 3a, but the particles are predominantly sideromelane basalt and K-rich particles from a more

296 evolved melt. These particles are highly angular and small, and show slight near-horizontal lineation
297 with larger particles being near the upper and lower bubble walls. There is clear sample preparation
298 damage to the upper bubble wall as labelled; (c) An area of extensive microlite chains within a
299 sideromelane clast from jökulhlaup sample Mul 6 unit 3a-1 8,000-16,000 2a (see Figure 2a for context).
300 The microlites (pink) occupy the upper right part of the image and coincide with small fragments of
301 various compositions. The lower left part of the image is void of microlites and particles but contains
302 near-spherical bubbles. The dashed line rectangles outline areas shown in Figures 8a and 8b.

303 3.3 Infilled bubbles

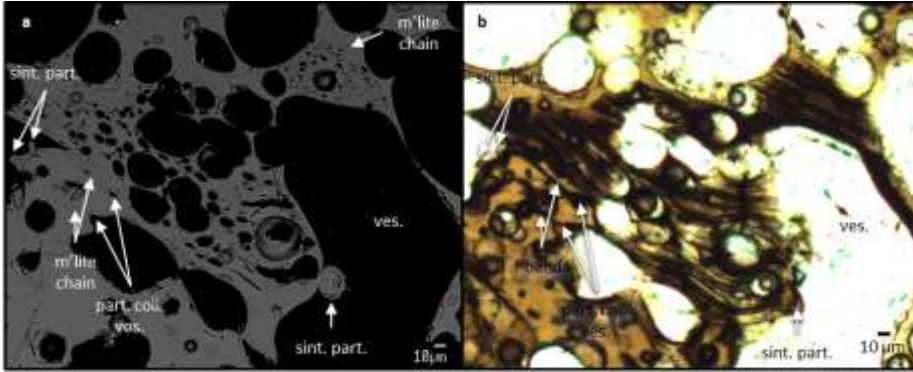
304 Interconnected bubble networks also frequently contain particles (Figs. 5b, 6). As with the fracture-
305 filling particles, these are predominantly angular, but include a significant proportion that are well
306 rounded and sintered onto bubble walls (Fig. 7).

307



308
309 Figure 6: BSE images showing examples (a and b) of particle-rich bubble chains in sideromelane
310 jökulhlaup clasts. In both examples, the bubble chain appears to widen as it approaches the clast
311 margin (upper right corner), however, the particles are most abundant at the opposite end. Particles
312 are predominantly absent from nearby isolated bubbles. (a) is from Mul 6 unit 2-1 8,000-16,000 2a
313 and (b) is from Mul 6 unit 3a-1 8,000-16,000 3a.

314



315

316 Figure 7: Images (a: BSE; b: ppl) showing sintered particles within bubbles in a sideromelane jökulhlaup
 317 sample - Mul 6 3a-2 8,000-16,000 2a (see Figure 2a for context). A round particle (~20 μm) is sintered
 318 to the wall of a large bubble (right side of the image), with a microlite chain marking the boundary. On
 319 the far left of the image is the edge of a bubble with two smaller sintered particles adhered to the
 320 bubble wall. The centre of the image is occupied by an area with a high number density of small
 321 bubbles, which appears flow-banded in part (b) and is outlined by a microlite chain. In the
 322 neighbouring glass beneath, there are partially collapsed vesicles, clearly visible in part (a), which
 323 pinch out into additional microlite chains; these also appear as flow bands in part (b).

324

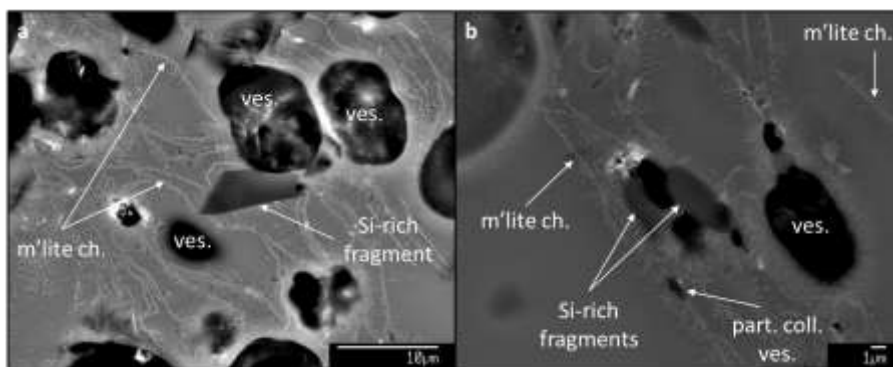
325 A compositional map was acquired within an irregular, highly deformed particle-filled bubble, which
 326 appears to form part of a series of interconnected bubbles (Fig. 5b). The particles are very small (<<63
 327 μm), generally angular and crudely sorted, with linear bands of finer grains in the bubble centre and
 328 larger particles on either side. The orientation of this band matches the orientation of the main axis
 329 of the bubble. The surrounding tachylite matrix consists of Ca-rich (green) and Fe- and K-rich (pink)
 330 microlites, which are most likely plagioclase, diopsidic pyroxene and Fe/Ti oxides (± orthopyroxene)
 331 typical of mafic magmas and Katla basalts (Lacasse et al., 2007; Budd et al., 2016). This phase
 332 assemblage contrasts with particles inside the bubble, which are predominantly either K-rich (blue)
 333 lithics, more likely belonging to a more evolved melt, or sideromelane (grey) juvenile glass particles.
 334 There are only two significant places where the particles match their host composition and their
 335 geometry suggests they are fragments of broken bubble wall and therefore are most likely a product
 336 of sample preparation (as labelled in Figure 5b). The foreign nature and the apparent sorting and
 337 imbrication of the remaining particles leads us to believe this is a magmatic feature.

338 3.4 High density microlite chains

339 The last compositional map (Fig. 5c) focused on an area containing abundant microlite chains within
 340 sideromelane. The microlite chains seem to connect crudely oval vesicles (Figs. 5c, 8), some of which
 341 appear partially collapsed (Fig. 8b). Many of the bubbles are surrounded by microlites (Fig. 8b). Various
 342 Fe-rich (red) and K-rich (blue) phases coincide with the location of microlite chains (Fig. 5c). These
 343 phases have both angular (Fig. 8a) and rounded (Fig. 8b) forms, suggesting that they are variably
 344 relaxed particles of a fragmented melt. The Fe-rich fragments (Fig. 5c) are either Fe-sulphides or Fe-Ti

345 oxides. The K-rich fragments (Fig. 5c) are likely feldspar (both alkali and plagioclase) and silicic glass.
346 EPMA analyses on select K-rich fragments reveal compositions consistent with dacite and plagioclase
347 feldspar (see section 3.8). K-rich particles within all the Figure 5 maps are therefore interpreted to be
348 fragments of silicic glass and/or crystal fragments derived from a more evolved melt. In contrast, the
349 lower left hand region in Figure 5c is almost devoid of both microlite chains as well as Fe/K-rich
350 particles and appears more vesicular with relatively large, near spherical bubbles.

351



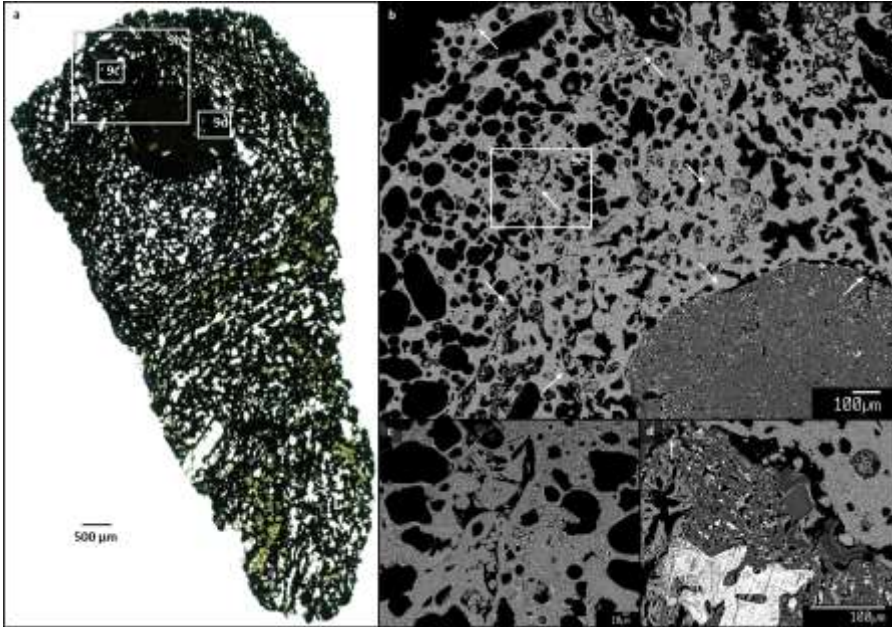
352

353 Figure 8: Images showing dark grey fragments of Si-rich material (revealed to be dacite and
354 plagioclase feldspar through EPMA spot analyses; see section 3.8 within a basaltic glass (pale grey)
355 riddled with microlite chains (white lines) and small bubbles (black), some of which appear partially
356 collapsed. This area has also been mapped compositionally (Fig. 5c) and the whole clast (jökulhlaup
357 sample Mul 6 unit 3a-1 8,000-16,000 2a) can be seen in Figure 2a. The Si-rich material appears in
358 both angular (a) and rounded (b) forms.

359 3.5 Other sintered textures

360 Sintering can be at times so extensive that it is unclear whether the original void was a bubble or a
361 fracture (Figs. 9, 10). In total, of the basaltic clasts for which there are BSE images, 12 of the 15
362 jökulhlaup clasts and 8 of the 9 air-fall clasts, show evidence of particle sintering.

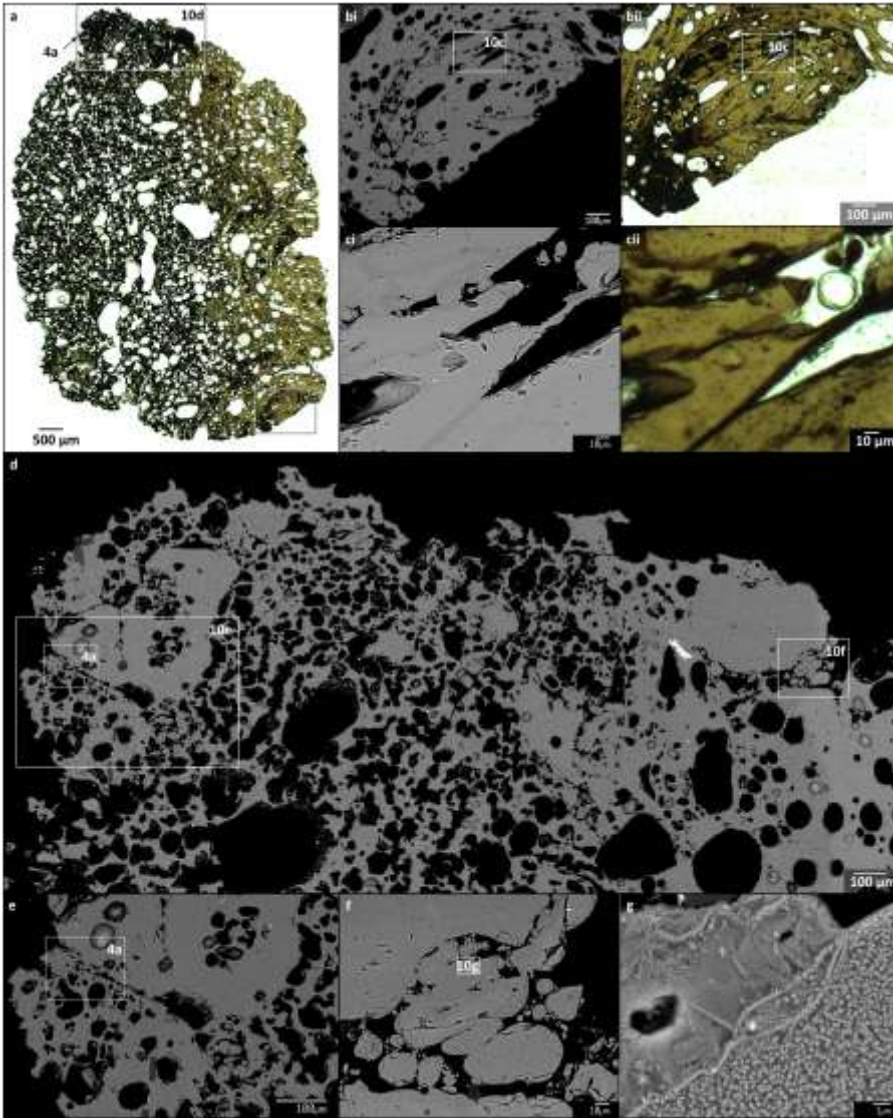
363



364

365 Figure 9: Images (in ppl (a) and BSE (b-d)) showing sintered particles within void spaces. The rectangles
 366 indicate areas detailed in other parts of this image as labelled. (a) Mosaic overview of the whole clast
 367 which is a tachylite jökulhlaup sample - Mul 6 unit 4-1 8,000-16,000 2a (~5x11 mm). There is a ~2 mm
 368 sized dark lithic in the upper part of the image and abundant particle filled bubbles, which appear pale
 369 brown in this image and appear to occupy distinct areas; (b) An overview of the upper part of the clast,
 370 with the lithic appearing dark grey in the bottom right hand corner. Bubbles (black) are nearly spherical
 371 on the left, but are significantly more irregular in the centre of the image. Irregular void spaces often
 372 coincide with sintered particles; particularly sintered areas are indicated with arrows; (c) An example
 373 of one of the highly sintered areas in part (b). The void in the image centre contains a large number of
 374 rounded particles; some of which are partially sintered onto the walls and others becoming
 375 indistinguishable from the matrix; (d) The boundary between the host clast (pale grey, upper right)
 376 and the lithic (dark grey) which contains a highly distorted phenocryst (white). There is a ~20 μm wide
 377 void space between the two enclosing rounded particles of tachylite, which in some cases are sintered
 378 onto the host clast.

379



380

381 Figure 10: Examples of sintering within the jökulhlaup clast Mul 6 unit 4-1 8,000-16,000 3a. (a)
 382 Photomicrograph mosaic image in ppl showing an overview of the whole clast (~6x9 mm), which is
 383 mixed tachylite (left) and sideromelane (right). Solid and dashed line rectangles express the areas
 384 shown in other parts of this figure and other figures, respectively, as labelled; (b) a semi-circular
 385 feature with a high abundance of rounded tachylite and sideromelane particles. It is unclear whether
 386 this was once a fracture which has welded shut or whether the whole area shows variably sintered
 387 clasts (i: BSE; ii: ppl); (c): detail of the area outlined in part (b) showing partially collapsed bubbles that
 388 contain rounded, sintered particles with microlite chains extending from the pinched point of each

389 vesicle. (i: BSE; ii: ppl); Parts d-g show BSE images of the upper part of the clast; (d) overview mosaic
390 image. The area shows extensive but heterogeneously distributed sintering. Arguably the large dense
391 areas in the upper left and right-hand corners could represent former large particles spanning several
392 hundred microns in diameter that have fused with the host. (e) and (f) illustrate the potential lower
393 boundaries of these larger former particles, with small sintered particles prominent in this void space.
394 The dashed rectangle in part e outlines the 'fracture' shown in Figure 4a. (g) Detail showing the
395 sintering interface between two rounded particles of tachylite, which is marked by a microlite chain
396 of oxides.

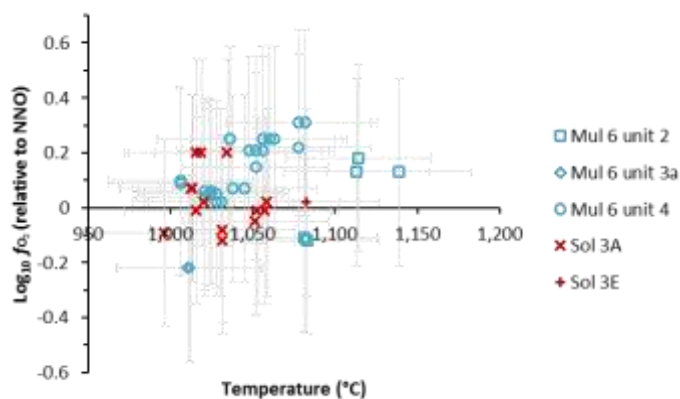
397

398 3.6 Geothermometry

399 Fe-Ti oxides yield an average temperature of $T=1,045 \pm 31$ °C (n=45 pairs) for K1918 basalts (Fig. 11).

400

401



402

403

404 Figure 11: Magma temperatures plotted against oxygen fugacity, estimated from magnetite and
405 ilmenite compositions using the model of Ghiorso and Evans (2008). NNO refers to a nickel-nickel
406 oxide oxygen buffer. Jökulhlaup and air-fall samples are prefixed by "Mul" and "Sol" and are coloured
407 blue and red respectively. The error bars represent average absolute deviation (44°C and 0.34 log units
408 for temperature and oxygen fugacity (f_{O_2}) respectively), calculated by Blundy and Cashman (2008) for
409 the Ghiorso and Evans (2008) model.

410 3.7 FTIR

411 One air-fall clast was measured and found to have a glass H₂O content of 0.08 wt.% (Table 1) consistent
412 with degassing to atmospheric conditions (e.g. Tuffen and Castro, 2009). K1918 jökulhlaup clasts have
413 glass H₂O contents of 0.15-0.31 wt.% (Table 1), consistent with a pressure elevated beyond

414 atmospheric, but not equivalent to the full weight of the glacier. Using the pressure-solubility model
 415 VolatileCalc (Newman and Lowenstern, 2002) and assuming a Si-content of 47 wt.% (consistent with
 416 Óladóttir et al. (2008)), 0 ppm of CO₂ (as measured) and a temperature of 1,045 °C (estimated using
 417 geothermometry; section 3.6), the jökulhlaup clasts likely quenched under 0.29-1.11 MPa of pressure.
 418 The loading pressure (P in Pa) can be estimated by multiplying gravity (g: 9.81 m s⁻²) by the density (ρ
 419 in kg m⁻³) and thickness of the load (h in m).

$$P = \rho gh \quad (2)$$

422 Thus a 400 m thick glacier (as was inferred to be the ice thickness over the vent in 1918 A.D.; (Sturkell
 423 et al., 2010)), with a density of 917 kg m⁻³ (Tuffen et al., 2010) would exert a pressure of 3.60 MPa,
 424 approximately four times greater, or more than the jökulhlaup clasts experienced syn-quenching.
 425 There is no systematic variation in H₂O content within the stratigraphic section sampled in Figure 1c.
 426 Therefore taking the average jökulhlaup glass H₂O content (0.22 wt.%), we can estimate that the
 427 average load during quenching was 0.59 MPa. This equates to approximately 65 m of ice, 60 m of
 428 water, 20 m of solid rock or 10 m of 50% vesicular basalt, assuming densities of 917, 1,000 and 2,770
 429 kg m⁻³ for ice, water and K1918 basalt respectively, with errors of ~20%. However, natural samples
 430 often experience loading by a combination of materials (Tuffen et al., 2010; Owen et al., 2012; Owen
 431 et al., 2013b; Owen, 2016; Owen et al., in press).

432

433 Table 1: FTIR results showing glass H₂O contents for five K1918 clasts.

Environmental Setting	Sample name	Mean H ₂ O content (wt. %)	Standard deviation (wt. %)	Number of successful analyses
Air-fall	Sol1A 8,000-16,000 4b	0.08	0.01	11
Jökulhlaup	Mul6 unit 2-1 8,000-16,000 2b	0.22	0.02	9
Jökulhlaup	Mul6 unit 2-1 8,000-16,000 4b	0.21	/	1
Jökulhlaup	Mul6 unit 4-1 8,000-16,000 1b	0.31	0.04	2
Jökulhlaup	Mul6 unit 4-1 8,000-16,000 4b	0.15	0.05	2

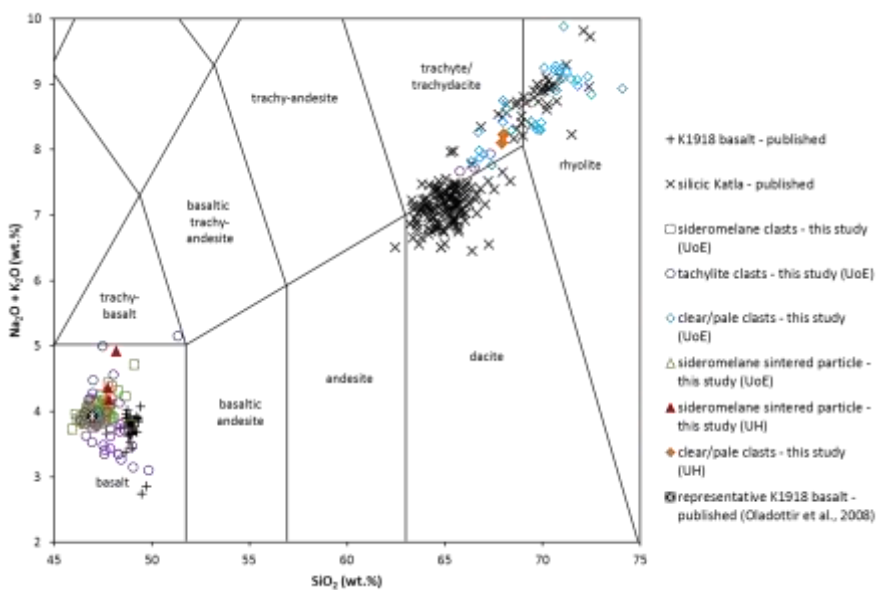
434

435 3.8 Geochemistry

436 There is strong consistency between the EPMA data gathered at the University of Hawaii, that
 437 gathered at the University of Edinburgh and that already published for Katla (Fig. 12). EPMA data (Fig.
 438 12) shows a bimodal distribution with sideromelane and tachylite clasts having ~47 wt.% SiO₂
 439 consistent with K1918 data published by Óladóttir et al. (2008), although the tachylite data is more
 440 scattered, likely due to these clasts being more microlite-rich (e.g. Fig. 4). In addition to the brown
 441 (sideromelane) and black (tachylite) clasts, most samples had a small percentage of clear/pale clasts

442 which have a trachyte/trachydacite to rhyolite composition consistent with older silicic Katla eruptions
 443 (Lacasse et al., 1995; Newton, 1999; Larsen et al., 2001; Lacasse et al., 2007; Óladóttir et al., 2008).
 444 Sintered sideromelane particles have similar compositions to the larger discrete sideromelane clasts
 445 (Fig. 12). Sintered K-rich particles found within an area of extensive microlite chains within a
 446 sideromelane clast (Fig. 5c) were found to have compositions consistent with plagioclase feldspar and
 447 dacite (Table 2). Although a relatively high Fe content (potentially from crystal contamination) meant
 448 they were excluded from Figure 12, they are also consistent with the published data from older silicic
 449 Katla eruptions.

450



451

452 Figure 12: A TAS plot of EPMA glass data from Katla showing published values (black) from K1918 and
 453 older silicic eruptions, as well as data from this study (colour). Clast types have been distinguished by
 454 colour either as brown sideromelane, black tachylite or clear/pale lithics. UoE (open symbols) and UH
 455 (filled symbols) denote the University of Edinburgh and the University of Hawaii respectively, which is
 456 a reference to the institution where the analyses were performed. 'Sintered particles' refer to small
 457 sintered particles within larger 'clasts'. Published K1918 data is from Óladóttir et al. (2008) and Budd
 458 et al. (2016) with the former used to represent K1918 geochemistry for density and solubility-pressure
 459 estimations. Published data of older silicic eruptions is from Lacasse et al. (1995), Newton (1999),
 460 Larsen et al. (2001), Lacasse et al. (2007) and Óladóttir et al. (2008).

461

462 Table 2: EPMA analyses of three particles within the area of extensive microlite chains in Figure 5c
 463 (sample Mul 6 unit 3a-2 8,000-16,000 2a). The analyses are consistent with the compositions of dacite
 464 (top two) and plagioclase feldspar (third analysis).

Field Code Changed

Analysis number	SiO ₂	TiO ₂	Al ₂ O ₃	FeO	MnO	MgO	CaO	Na ₂ O	K ₂ O	P ₂ O ₅	Cl	TOTAL	Inferred material
1	63.76	1.85	13.45	7.39	0.16	1.31	4.19	2.09	2.31	0.21	0.08	96.79	dacite
2	65.70	1.67	14.83	6.66	0.15	1.35	3.64	4.13	2.17	0.21	0.07	100.57	dacite
3	54.45	0.33	28.60	1.40	0.00	0.29	11.33	4.99	0.23	0.00	0.00	101.63	plagioclase feldspar

465

466 4. Discussion

467 4.1 Evidence of gas and ash transport within permeable pathways

468 Many of the samples contain fractures and/or have connected bubbles, some of which contain small
469 particles of fragmented material. It is possible for such features to form during poor sample
470 preparation. Grinding during thin section making may fracture the rock, break thin bubble walls
471 connecting vesicles and produce small particles which may then lodge in void spaces. It is also possible
472 for fractures to form during quenching. However, both cooling-contraction cracks and sample
473 preparation cracks should be brittle as they happen < T_g, whereas most of our observed fractures
474 show ductile morphologies (Figs. 3b,4,5a), suggesting they experienced temperatures > T_g. Also, we
475 would expect particles distributed during sample preparation to be random. However, what we have
476 observed in the K1918 deposits is a very organised distribution of particles throughout the clasts.

477 Most of the particles are found in fractures and bubbles that are connected, and rarely within isolated
478 bubbles (Figs. 2-6). When particles do occur in apparently isolated bubbles, they are often in close
479 proximity to a bubble chain (e.g. Figs. 2c, 6a) and we suspect that they are actually connected in the
480 third dimension. Figure 9 shows clear areas of infilled bubbles and clear areas with none. These
481 distribution patterns are hard to explain with poor sample preparation. Furthermore, the particle filled
482 bubble in Figure 5b seems to show layering parallel to the axial plane of the bubble, consistent with
483 clastic deposition of particles within a stream of gas, as documented in silicic tuffisite veins where
484 internal laminae are parallel to fracture walls (Tuffen et al., 2003).

485 What is more, compositional maps (Fig. 5) reveal that within both fractures (Fig. 5a) and bubbles (Fig.
486 5b) the phase assemblage and composition of the particles is at least partly distinct from that of the
487 host, yet consistent with K1918 textures and geochemistry. All three compositional maps in Figure 5,
488 reveal silicic particles and felsic crystal fragments that have compositions consistent with older silicic
489 eruptions (Fig. 12). It is most likely that particles introduced through grinding in thin section
490 preparation would be exclusive to the host. In Figure 5b, there is almost a 100% inconsistency; there
491 are only a few particles consistent with the composition and textures of the tachylite host, with the
492 vast majority being particles of silicic and basaltic glass. We hypothesise that based on the tachylite
493 particles being in close proximity to the host and with a jigsaw like fit, that these particles *do* represent
494 poor sample preparation. However, the vast majority of the particles cannot be explained by this and
495 we speculate that they are a primary feature.

496 The presence of sintered particles (Figs. 4,5a,7,9,10) is further evidence that particle deposition was a
497 syn-eruptive process as sintering suggests that some of the particles experienced temperatures > T_g
498 within the fractures/connected bubbles. Some fractures and particle-particle contacts are almost fully
499 healed (e.g. Fig. 4b), making it difficult to deduce the original fracture wall or particle boundary (e.g.
500 Fig. 5a). Therefore, fractures may have been wider than currently observed. The presence of K-rich

501 particles, collapsed vesicles and microlite chains in the host immediately surrounding the fracture in
502 Figure 5a further supports this notion. This thorough healing and compaction is analogous to welded
503 rhyolitic tuffisites (Tuffen and Dingwell 2005).

504 Furthermore, there are textures consistent with clast re-amalgamation; Figures 9 and 10, seem to
505 show former clasts embedded within larger clasts, with small particles sintered to the former clast
506 walls and to each other, within boundary zones (Figs. 9d, 10f). This is germane to tuffisite vein interiors
507 (Saubin et al., 2016) again suggesting larger permeable pathways than the preserved features.

508 Evidence for volatile transportation can be seen as local heterogeneity in bubble textures. We
509 speculate that the vesicle-poor area neighbouring the fracture in Figure 4b failed to vesiculate as much
510 as the surrounding glass due to volatile depletion following diffusive loss into the degassing fracture
511 (see section 4.6). Similar textures have been observed in rhyolitic Chaitén bombs (Saubin et al., 2016;
512 Webb et al., 2017).

513 We therefore hypothesize that bubbles (Figs. 5b,7,9) and fractures (Figs. 2,3,4,5a) have acted as
514 pathways for the transportation of both juvenile and lithic material, analogous to tuffisite veins in
515 silicic pyroclastic material (Rust et al., 2004; Saubin et al., 2016). Systematic transport is shown by the
516 organised distribution of particles and was likely facilitated by gas flow evidenced by diffusive loss
517 shown by the apparent vesicularity gradient surrounding the fracture in Figure 4b. Ductile fracture
518 morphologies and sintering suggest that both the fractures and particles within them experienced
519 temperatures $> T_g$ and thus we believe it to be a syn-eruptive process that likely occurred within the
520 conduit.

521 4.2 Evidence of former gas and ash transport within healed permeable pathways

522 Partially collapsed vesicles surround many of the features of interest e.g. the fracture in Figure 5a, the
523 vesicles containing sintered particles in Figure 7, the area of intense microlite chains and Si-rich
524 particles in Figure 8 and the sintered particles in Figure 10c. These collapsed vesicles always transition
525 into microlite chains (Figs. 5a, 7, 8b and 10c). Furthermore, the bubbles in Figure 8b are surrounded
526 by microlites. Thus, we believe some of the microlite chains to represent healed vesicles.

527 Microlite chains also seem to have formed between sintered particles (e.g. Figs. 4ai and 10g).
528 Arguably, the similarity in size and morphology of the microlite chains in Figure 5a to the intra-fracture
529 particles could mean that they represent the boundaries of former particles that have since melted
530 into the surrounding host.

531 Whether microlite chains represent collapsed vesicles (e.g. Fig. 8b) or the margins of former particles
532 (e.g. Fig. 10g), they represent healed void-spaces. This is further evidenced by the relatively high S
533 content (Fig. A1) of the microlite chains surrounding the fracture shown in Figure 5a. Furthermore, it
534 suggests that these facilitated volatile transport with vapour-phase precipitation occurring on former
535 fracture/bubble/clast walls. In fact, in compositional maps, the microlite chains often appear similar
536 in colour to partially exposed bubbles (Fig. 5). The coincidence of these microlite chains with silicic
537 particles (e.g. Figs. 5c, 8) suggests that these healed voids also transported particles. Thus, we believe
538 the dense area of microlite chains and foreign particles in Figure 5c to show a healed transport
539 pathway for a particle-rich fluid phase.

540 There is an apparent compositional similarity between the matrix delineated by these microlite chains
541 and the surrounding microlite-free host basalt glass (Fig. 5c). However, the compositional maps shown
542 in Figures 5a and 5b indicate that basaltic fragments make up the majority of fragmented particles.
543 Therefore, it is likely that the permeable pathways that carried the K-rich particles in Figure 5c, also
544 transported basaltic particles. Evidence for this comes from the fragment of anorthitic plagioclase in
545 Figure 5c; an An-rich plagioclase likely has a mafic source. Apart from the mineral fragment, the basalt
546 is now indistinguishable from the host and therefore likely juvenile in origin. This suggests that Figure
547 5c represents a juvenile magma that fragmented (along with a minor percentage of felsic origin) and
548 was then transported in a permeable pathway, which then collapsed and healed. Small vesicles then
549 grew in the scarred remains (Fig. 8).

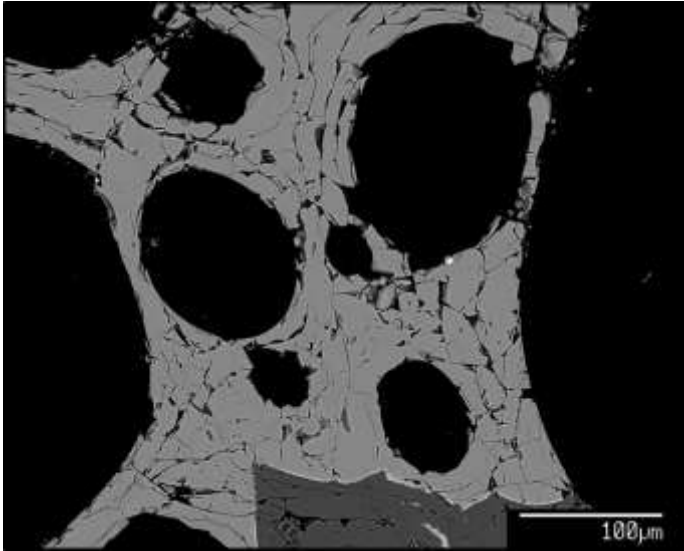
550 Microlite chains also often surround fractures/permeable pathways (Figs. 5a, 10) indicating that they
551 may have partially healed. However, in Figure 5a, there are K-rich particles embedded into the basaltic
552 glass even beyond the zone of microlite chains surrounding the particle-filled fracture. This is evidence
553 of near complete healing. The apparent progressive welding around Figure 5a suggests that the
554 fractures were once considerably wider than they appear in some of the images; this healing of
555 pathways is akin to tuffsite veins (Tuffen et al., 2003).

556 4.3 Origin of the basaltic particles

557 Most of the bubble- fracture- filling particles have compositions consistent with K1918 basalt (Figs. 5
558 and 12) suggesting that it is juvenile material. This suggests that at least two fragmentation events
559 were involved in the production of the K1918 clasts: firstly to produce the small particles, which are
560 now trapped in the clasts, and lastly to produce and expel the clasts that were sampled. Sintering and
561 healing is apparent between these two events and it is possible that there were further fragmentation
562 events, however the rapid sintering rates of basalt makes it difficult to deduce how many
563 fragmentation events occurred in total.

564 The fact that the first fragmentation event did not expel the particles, suggests that it may have
565 happened within the conduit, but at shallow level owing to the low H₂O contents (Table 1), low
566 vesicularities of the particles (Figs. 2-10) and incomplete sintering (Figs. 2-10), suggestive of short
567 residence times (see below).

568 Some clasts also show evidence of incomplete fragmentation (fracturing without significant
569 displacement or expulsion) and brittle deformation (Fig. 13). The fragments of glass between the
570 fractures share similar sizes, morphologies and vesicle textures to the fracture and bubble filling
571 particles seen throughout the samples (e.g. Figs. 5, 6). This sample therefore represents an inefficient
572 fragmentation event which failed to expel particles. It is likely linked with one of the early
573 fragmentation events that produced fragments of glass that then infiltrated the remaining melt
574 through connected bubbles and fractures.



575

576 Figure 13: A BSE image showing highly fractured sideromelane within jökulhlaup sample Mul 6 unit 4-
577 1 8,000-16,000 1a, which could have acted as a source for small particles that later sintered with
578 fractures and bubbles elsewhere (e.g. Figs. 5, 6). The dark grey shape at the bottom is a phenocryst.

579 4.4 Origin of the felsic particles

580 Although the majority of particles are basalt, every compositional map (Fig. 5) revealed the presence
581 of some K-rich particles which spot analyses indicated were fragments of feldspar and dacite (Table
582 2). Clear/pale clasts were also found to have compositions of a more evolved melt consistent with that
583 of older silicic Katla eruptions (Fig. 12) (Lacasse et al., 1995; Newton, 1999; Larsen et al., 2001; Lacasse
584 et al., 2007; Óladóttir et al., 2008). In fact, there are extensive silicic outcrops within the Katla caldera,
585 including some close (<4 km) to the inferred 1918 A.D. vent (Jóhannesson and Sæmundsson, 2014).
586 We therefore hypothesize that the glassy K-rich particles represent fragments of evolved country rock
587 (dacite, trachyte/trachydacite and rhyolite) that were mobilised during fragmentation and
588 incorporated into connected fracture-bubble networks by a mobile fluid phase during ascent. This
589 possibility was recognised by Budd et al. (2016) who used mineral-melt equilibrium crystallisation
590 pressures to infer multiple magma storage regions at Katla with the potential for new rising magma
591 to intersect evolved magma within shallow-storage regions.

592 4.5 Particle morphology, sintering timescales, and link with composition

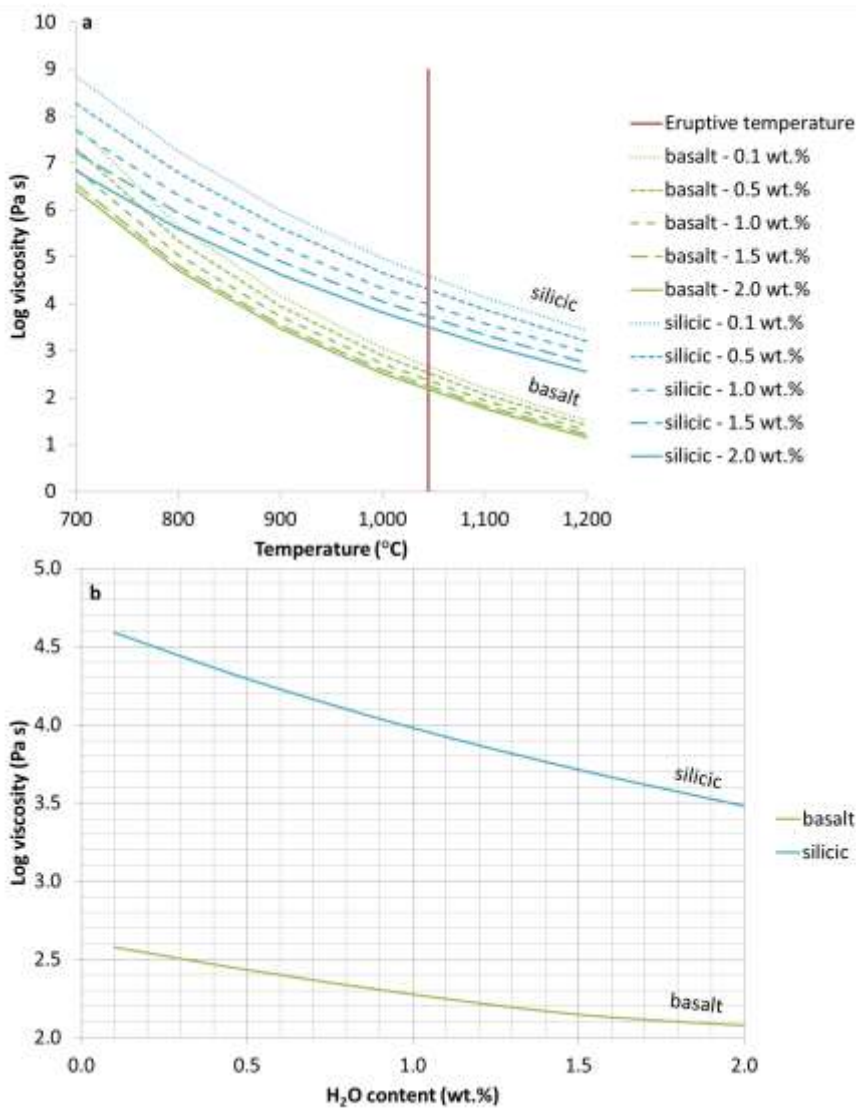
593 The morphology of the silicic particles is generally angular, in contrast to the basaltic particles, which
594 are more often rounded (Fig. 5a). Within magmatic fractures that appear to have largely healed, the
595 angular morphology of glassy silicic lithics (Figs. 5c & 8a) is surprising, as surface tension-driven shape
596 relaxation would occur rapidly at basaltic eruptive temperatures.

597 We consider two possible explanations for why the silicic particles are generally less deformed than
598 basalt ones (Fig. 5a). Firstly, even though the Si-rich material was considerably hotter than its usual

599 eruptive temperature, it would still have had a significantly higher viscosity than the basalt (Fig. 14)
600 and therefore the timescales for deformation, shape relaxation and sintering would have been
601 considerably longer (Vasseur et al., 2013). Secondly, being part of the country rock, the silicic material
602 was likely incorporated at far lower temperatures than the juvenile basalt (1,045 °C), and would thus
603 have needed to first rise to temperatures >T_g in order to deform, further hindering sintering.

604

605



606

607

608 Figure 14: viscosity as a function of composition, temperature and H₂O content, according to the
609 viscosity model of Giordano et al. (2008). For the 'basalt' and 'silicic' composition the analyses that
610 most closely resembles published data was used (Fig. 12). The red line depicts our inferred eruptive
611 temperature (1,045 °C). (a) viscosity plotted against temperature, for different compositions (colours)
612 and H₂O contents (line styles); (b) viscosity plotted against H₂O concentration for our inferred eruptive
613 temperature of 1,045 °C.

614 To investigate these two scenarios, and to produce some crude estimates of heating, relaxing and
615 sintering timescales, we performed some basic first-order estimations (Appendix 2). The results show
616 that owing to the small particle size, all of the intravoids particles shown in this study (typically << 100
617 µm) would have likely reached thermal equilibrium within milliseconds (Fig. A4). The time taken to
618 heat silicic particles (of this size) to basaltic magmatic temperature therefore seems insignificant.

619 Our inferred rounding/sintering timescales are only slightly longer (fractions of seconds) than
620 timescales for thermal equilibrium, but are strongly viscosity-dependent (Vasseur et al., 2013). We
621 therefore conclude that the rounding/sintering rate is the main process that controlled particle shape.
622 Even at 1,045 °C, which is significantly higher than its usual eruptive temperature, the viscosity of the
623 silicic magma will be high enough to extend the rounding/sintering timescale by one or two orders of
624 magnitude compared to basalt (Fig. A5). Consequently, for particles of comparable size, the basaltic
625 particles can thoroughly sinter and heal before the silicic particles have relaxed to a rounded shape.
626 These viscosity-controlled differences in rounding/sintering rate can therefore explain the angularity
627 of silicic particles within a healed matrix of basalt in Figure 5c, and the apparent deformation of a
628 basaltic particle around a similarly sized angular silicic particle in Figure 5a.

629 Estimating exact sintering times is difficult since timescales are extremely sensitive to composition,
630 H₂O content and particle size (Fig. A5). These parameters will also be changing throughout the process,
631 and it is difficult to deduce the original starting conditions from what is preserved in the samples
632 (Pope, 2015).

633 Nevertheless, our basic calculations (Appendix 2) suggest that the sintering times, for the preserved
634 particles within the fractures/bubbles/voids, was at most a few seconds. Any longer would have likely
635 resulted in complete healing. For angular clasts, this process would have been even quicker, and/or
636 the particles were injected below T_g; either way suggests near instantaneous injection, fragmentation
637 and quenching. The fact that some of the voids contain both angular and rounded particles of similar
638 sizes (e.g. Fig. 5a) suggest that there was momentarily a stream (albeit very short-lived) of gas and ash
639 with particles entering the space at slightly different times.

640 Final quenching was likely closely linked with fragmentation at Katla. Fragmentation may have even
641 been triggered or enhanced by melt-water interaction. Even if not phreatomagmatic, located under a
642 glacier, there would have been abundant ice and meltwater present in close proximity to the vent.
643 FTIR analyses reveal that the jökulhlaup samples quenched under pressures consistent with loading
644 from ice or water (see section 3.7). The glassy nature of the sideromelane also implies rapid
645 quenching.

646 It should be noted that the inferred residence time of variably sintered particles is not necessarily an
647 indicator of the full duration of void opening. These voids, when first opened, may have been vapour-
648 rather than particle-filled. Additionally, small (<100 µm) basaltic particles will fully sinter very rapidly
649 (in fractions of seconds; Fig. A5), after which it will be difficult to recognise the former presence of
650 particles. Some fractures are neighboured by K-rich fragments, collapsed vesicles and microlite chains
651 that form crude particle-shaped patterns (Fig. 5a). We hypothesise that these textures represent
652 former particles that fully annealed to the void walls, and that microlite chains often indicate former
653 permeable pathways/healed voids (e.g. Figs. 5c, 8; see section 4.2). However, it is difficult to
654 determine the extent of healed pathways, because chemical diffusion and viscous flow will
655 homogenise the sintered melt, ultimately leaving little/no trace of the former particle boundaries. For
656 these reasons, we suggest that the voids were open over seconds, and only the final split seconds of
657 the void life is preserved within our samples. We hypothesise that the preservation (particularly of
658 angular particles) was possible due to rapid quenching in water, which must have occurred almost
659 simultaneously with the final injection of particles. This indicates a very rapid succession of
660 deformation that was brittle (to form the initial particles), ductile (to sinter the particles) and then
661 brittle again (to expel and quench the particles).

662 4.6 Diffusive loss of volatiles through fractures, and timescale for open system degassing

663 To further investigate the lifetime of the permeable networks we provide estimates of diffusion
664 timescales (Appendix 3). There are several lines of evidence that permeable networks have facilitated
665 diffusive loss of volatiles. Firstly, microlite chains and bubble walls are usually S-rich (Figure A.1). These
666 microlite chains were likely former voids and particle boundaries (see section 4.2), where S-rich gases
667 circulated and deposited along the suture zones. Secondly, the glass surrounding some of the voids
668 (e.g. Figure 4b) is noticeably deficient in terms of bubble textures compared to the surrounding melt.

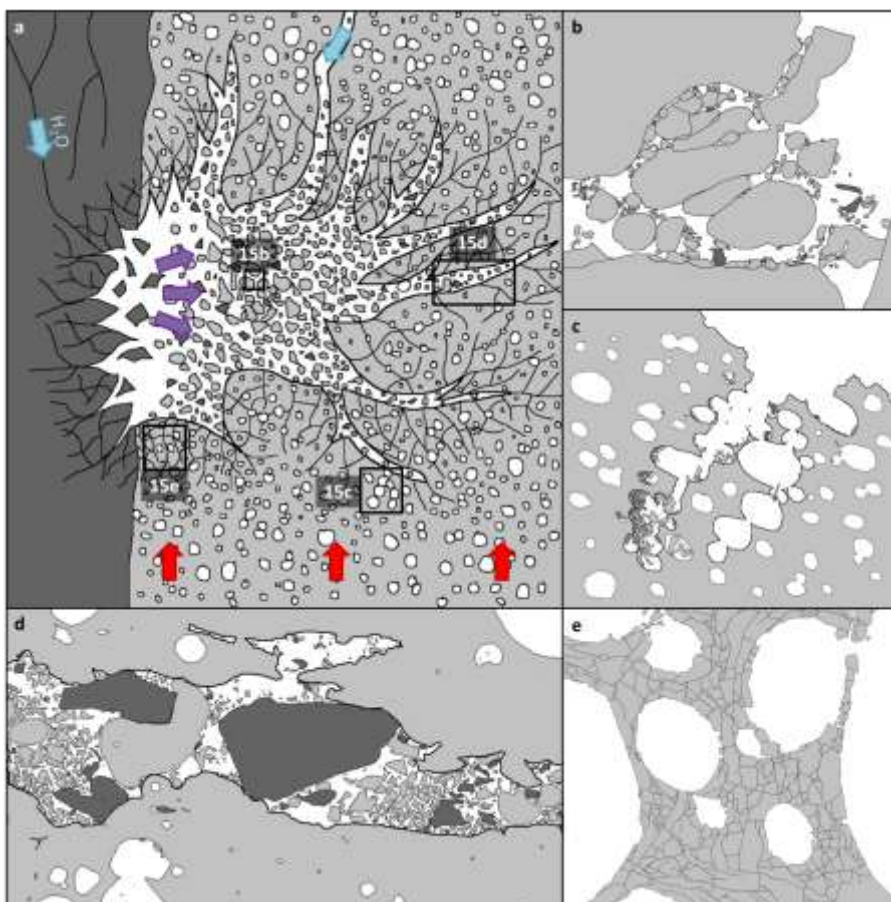
669 Bubble-poor, fracture-adjacent basaltic glass could indicate diffusive volatile loss into the void-space.
670 If a low pressure void opens within magma, it will allow volatile escape, drawing H₂O out of the melt
671 through diffusion. Subsequent decompression of the melt during ascent, will then yield lower
672 vesicularities than surrounding melt which has not experienced diffusive loss (Saubin et al., 2016;
673 Webb et al., 2017). Furthermore, the vesicularity and bubble size of particles within the Figure 4b
674 fracture are extremely similar to the glass adjacent to the fracture. This further supports the notion of
675 diffusive loss and suggests that the glass within and immediately surrounding the fracture was able to
676 diffuse to a similar H₂O concentration which was lower than the host melt, prior to the final
677 vesiculation event.

678 Using 1D diffusion calculations to quantify the development of an 80 µm wide H₂O depleted zone
679 (Appendix 3), we estimate that the fracture shown in Figure 4b experienced volatile loss by diffusion
680 towards the melt-fracture interface for ~40 seconds. This particular fracture has been extensively
681 healed. We therefore infer that the pre-quenching lifetime of other less-sintered fractures (e.g. Figs.
682 4a, 5a, 10) was much shorter. Our diffusion timescales are therefore close to timescale estimates for
683 sintering and residence times of inter-void particles discussed in the previous section. Nevertheless,
684 there is clearly a range of sintering and quenching timescales preserved within those clasts, as
685 expected in fragmented magma with a wide range of grainsizes and textures.

686 4.7 The nature of the void spaces

687 Small particles occupy many different void spaces e.g. angular fractures (Fig. 2), rounded fractures
688 (Fig. 3), tuffisite vein-like features (Fig. 4, 5a), bubbles and bubble chains (Figs. 5b, 6, 7) and the
689 boundary space between sintered clasts (Figs. 9, 10). At times, the sintering is so extensive that it is
690 difficult to deduce the original void shape (Fig. 9c). For instance, some features could be interpreted
691 as a vein-like fracture (Fig. 4a) or a boundary zone between clasts (Figs. 10d, 10e). Nevertheless, there
692 is textural and compositional evidence for gas and particle transfer in fractures, bubble chains and
693 sintered breccias (often in the same clast; Figures 2a, 10a), and in reality, all are likely to occur, as they
694 do in rhyolitic magma (Stasiuk et al., 1996; Schipper et al., 2013).

695 We propose a hypothetical model where localised explosions fragment both the country rock and
696 some of the juvenile material, which are jetted into fractures, vesicles and mobile breccias, either
697 moments before or during ejection from the vent (Fig. 15).



698
699 Figure 15: Our interpretative model to explain the various textures seen within the K1918 clasts. In (a)
700 a vesicular basaltic melt (pale grey) is rising next to older silicic country rock (dark grey) from past Katla
701 eruptions. A small localised explosion, either caused by magmatic fragmentation, or more likely

702 phreatomagmatic fragmentation from H₂O percolating down through cracked country rock, shatters
703 both the silicic country rock and the neighbouring basaltic melt. This creates a hot mobile phase of
704 particles which begin to sinter together (b), infiltrate chains of connected bubbles (c) and infiltrate the
705 transient fractures formed by the explosion (d). The melt surrounding the blast zone has been
706 shattered (e) representing an incomplete version of the fragmentation within the blast zone. These
707 features, would have only existed for, at most, seconds before thorough welding took place.
708 Preservation requires further fragmentation to expel and quench the clasts into a water-rich
709 environment, which was perhaps facilitated by meltwater percolating down through cracks in the
710 damaged magma and wall rock. Parts b, c, d and e represent Figures 10f, 6a, 5a and 13 respectively.

711

712 4.8 Comparisons with rhyolite-hosted tuffisite veins

713 Tuffisite veins are the quenched remains of fractures that form in silicic melts, which allowed a
714 pathway for gas and ash particle transport. As described in the previous section, it is unclear whether
715 some of the K1918 textural features represent true 'veins', bubble chains or inter-clast spaces; we
716 appear to have a spectrum of void spaces that include all end-members. Nevertheless, these samples
717 clearly show evidence of permeable pathways for gas and ash particle transport, that heal shut with
718 time in repeated fragmentation cycles (Fig. 15) analogous to tuffisite veins.

719 The circulation of gas through a permeable network is clear from S-rich microlite chains (Fig. A1) and
720 gradients in bubble textures surrounding voids (Fig. 4b). The mobilisation of particles is demonstrated
721 by the systematic distribution of particles within clasts (Figs. 2c, 6a, 9a) as well as bedding within
722 bubbles (Fig. 5b), which was also reported in rhyolitic tuffisites from Torfajökull (Tuffen et al., 2003).
723 Furthermore, foreign particles (silicic particles within basalt (Figs. 5a, b and c) and sideromelane
724 particles within tachylite (Fig. 5b)) must have been transported to their current location. Transport
725 clearly happened at magmatic temperatures because numerous particles show evidence of
726 rounding/sintering, which is also a feature of rhyolitic tuffisites (Tuffen and Dingwell, 2005).

727 The inter-void particle size in the K1918 clasts (10-200 µm diameter) is similar to those found in
728 tuffisite veins and, like rhyolitic tuffisites, angular fragments dominate over rounded ones (Tuffen et
729 al., 2003; Tuffen and Dingwell, 2005). It is difficult to compare the size of the fractures themselves. In
730 rhyolite tuffisite veins can be > 5 m (Tuffen et al., 2003) or < 100 µm (Saubin et al., 2016). The fractures
731 we observed tended to be tens of µm in width (Figs. 4 and 5). We suspect that pathways were once
732 bigger and have narrowed through welding processes (section 4.2) but it is also worth noting that our
733 observations were limited to small particles (<16,000 µm). This begs the question; were the permeable
734 pathways in the K1918 basalt limited to a small size, or did significantly larger fractures exist, and have
735 been destroyed by the explosive nature of this eruption? Indeed the sintered breccia in Figure 10 could
736 be evidence for a larger scaled feature, as are the xenoliths trapped within clasts (e.g. Fig. 9). Perhaps
737 the whole conduit was acting as a permeable pathway for fragmentation and sintering.

738 However, there is one clear difference; the permeable pathways in the K1918 basalt seem to be much
739 more transient than rhyolitic tuffisites. Thermal (Appendix 2) and diffusion (Appendix 3) estimates
740 suggest that the K1918 fractures were open for just seconds before quenching, whereas inferred
741 tuffisite vein lifetimes in rhyolite span ~10³-10⁵ seconds (Castro et al., 2012). This difference can be
742 explained by the lower melt viscosities and higher H₂O diffusivities that will occur in the hotter basaltic

743 system. Interestingly, however, diffusion distances are similar; typically tens to a few hundred μm
744 (Castro et al., 2012; Berlo et al., 2013; Saubin et al., 2016).

745 4.9 Links with eruptive behaviour

746 In silicic systems, permeable pathways in magma (whether connected bubbles or tuffisite veins) often
747 serve to enhance magma degassing and outgassing, and may contribute to a transition towards more
748 effusive activity (Jaupart and Allègre, 1991; Jaupart, 1998). Permeable outgassing is also thought to
749 occur during subglacial volcanism and contribute towards transitions in eruptive behaviour (Owen et
750 al., 2013a; Owen et al., 2013b; Owen, 2016). Whilst the K1918 samples show plenty of visual evidence
751 for permeable pathways (Figs. 2-10), evidence of an effusive phase is lacking from the 1918 A.D. Katla
752 eruption, although deposits from such a phase could be obscured under the present glacier (Owen,
753 2016). Nevertheless, the clasts collected were small fragments from the large-volume jökulhlaup
754 deposit that originated from explosive fragmentation. In rhyolitic melts, tuffisite veins *alone* are
755 thought to be inefficient at degassing and outgassing magma, with spacing of $< 1\text{mm}$ required to
756 outgas the magma sufficiently to cause the transition to effusive behaviour (Castro et al., 2012).
757 Therefore, it is possible that the magmatic fractures observed within the K1918 samples were simply
758 insufficient to degas the magma efficiently. However, tuffisite veins that intersect permeable foams
759 *are* considered a highly efficient mechanism of magma degassing, and may induce a transition to
760 effusive behaviour, e.g. at Chaitén (Castro et al., 2012; Saubin et al., 2016). A large proportion of
761 bubbles within the K1918 samples contain ash particles. Therefore, gas was presumably transported
762 in connected bubbles as well as fractures (e.g. Fig. 6). If exsolved volatiles were able to efficiently
763 outgas why was the eruptive style so explosive?

764 One explanation could be the extremely transient nature of the permeable pathways in the basalt.
765 Simple calculations to estimate sintering (Appendix 2) and diffusion (Appendix 3) timescales suggest
766 vein lifetimes of seconds or less, approximately five orders of magnitude shorter than in rhyolitic
767 systems (Fig. A5) (Castro et al., 2012). However, diffusion in basalt would have also been fast, and our
768 inferred diffusion profile is of similar length scale to those seen in rhyolite (Castro et al., 2012).

769 An alternative model is that the permeable pathways (fractures and connected bubbles), in the K1918
770 magma, potentially served as mechanisms for enhancing explosivity rather than to defuse the
771 eruption. There are two explanations for this: (1) the pathways connected shallow magma to that of
772 a deeper source, allowing gas to be transported up from depth and thus adding to, rather than
773 reducing the volatile content of the fragmenting magma (Houghton and Gonnermann, 2008; Castro
774 et al., 2012); (2) the pathways allowed meltwater (from the overlying melting glacier) to efficiently
775 infiltrate into the magma column, facilitating fuel coolant interaction (FCI) and thus explosive
776 fragmentation.

777 The former, has been used to explain periods of heightened activity at Stromboli where open system
778 degassing brings high levels of CO_2 from a deep magma source (Allard, 2010). However, if this was the
779 case, one would expect volatiles to diffuse from the fracture into the melt and thus for the magma
780 adjacent to fractures to be volatile-rich compared to the surrounding melt. We saw no evidence for
781 this in our samples. In fact, if anything the opposite is true, as there is an apparent bubble-poor zone
782 around the fracture in Figure 4b.

783 It is more likely that the permeable pathways served to enhance fragmentation by meltwater
784 infiltration from the overlying glacier triggering FCIs. Abundant meltwater would have been present
785 at the time of the eruption and there is evidence that the jökulhlaup samples quenched under loading
786 from water/ice (section 3.7). The microlite-poor nature of the glass also suggests rapid cooling.

787 We therefore propose the following hypothesis to explain the sintered permeable pathways (Fig. 15):
788 1) rising vesicular magma melted overlying ice producing water; 2) As the magma neared the surface
789 it began to fragment (Fig. 15a). It is difficult to underpin the initial cause of the fragmentation; some
790 of the clasts are highly vesicular with high bubble number densities which could indicate magmatic
791 fragmentation but there would have also been abundant meltwater which could have filtered down
792 to the magma through cracks triggering phreatomagmatic fragmentation. Nevertheless, this
793 fragmentation event did not expel the melt fragments but instead injected them (Fig. 15b) into
794 connected bubbles (Fig. 15c) and fractures (Fig. 15d) in the remaining intact melt. The blast also
795 fragmented country rock which also got incorporated into these permeable pathways; 3) the hot
796 magma induced sintering of the particles and some of the pathways partially or fully healed; 4) only
797 seconds (or fractions of seconds) later, a further explosive event expelled the now fully fragmented
798 magma out of the vent into a watery environment inducing rapid quenching. The cause of this
799 fragmentation event was likely meltwater infiltrating the now highly fragmented magma through the
800 permeable pathways created by the first fragmentation event; 5) this explosion likely produced more
801 small particles and opened further fractures, allowing more meltwater to infiltrate the conduit in a
802 self-fuelling and repeating process with a cycle of seconds or less.

803 Repeating fragmentation events (Fig. 15) not only explain the particle filled void spaces but the
804 apparent clasts welded within clasts (e.g. Fig. 9). Our model (Fig. 15) could also help to explain why
805 the K1918 eruption was so powerful; magma-water mixing massively promotes fuel coolant
806 interactions (Zimanowski et al., 1991; Morrissey et al., 2000), and meltwater ingressed within
807 permeable pathways would have allowed plenty of opportunity for this. It could also explain why the
808 glacier melted so quickly and produced such a powerful flood; if the under-side of the glacier is
809 constantly being bombarded with a hot slurry of fine particles there will be both mechanical erosion
810 as well as rapid thermal melting from the large-surface area to volume ratio.

811 Finally, our model (Fig. 15) may help to explain why the sintering textures have been preserved so
812 well, particularly in the jökulhlaup clasts; abundant meltwater, perhaps also within the permeable
813 pathways would promote rapid quenching. The jökulhlaup samples, unlike the air-fall samples, also
814 show that they quenched under elevated pressure (section 3.7), which could perhaps be explained by
815 being emplaced into water, which would ensure the continued quenching of the particles and the best
816 preservation of features. Note that although there is evidence of sintered particles within the air-fall
817 samples, all of the best examples of particles sintered within permeable pathways were found in the
818 jökulhlaup clasts.

819 4.10 The extent of the permeable network within Katla 1918 pyroclasts

820 Sintered particles perhaps present the best evidence for clast transportation around the glass
821 transition and therefore the presence of a permeable network within the K1918 magma. Although
822 sintering is present in 80% of the K1918 clasts examined, rounded particles only make up a very small
823 percentage of the bubble and fracture-filling particles, which are predominantly angular (e.g. Figs.
824 5,6). When particles are angular, infilling could be thought of as an artefact of poor thin section

825 preparation (e.g. lack of sufficient ultrasonic cleaning to rid the sample surface of adhering ash).
826 However, the layered structures and exotic compositions, in Figure 5b, consistent with older silicic
827 Katla magma (Fig. 12 and section 4.2) emphatically indicate that these are primary textures. As the
828 particles in Figure 5b are almost exclusively angular, this conclusion can potentially be applied to all
829 infilled bubbles and fractures (regardless of particle morphology) which are found in a significant
830 proportion of all K1918 clasts (e.g. Fig. 9a).

831 Similarly, it is easy to quickly dismiss angular fractures as a feature formed through quenching or
832 sample damage during thin section preparation. However, even the angular fractures contain particles
833 favourably over nearby isolated bubbles (Figs. 2c, 3b, 6) suggestive of permeable pathways.

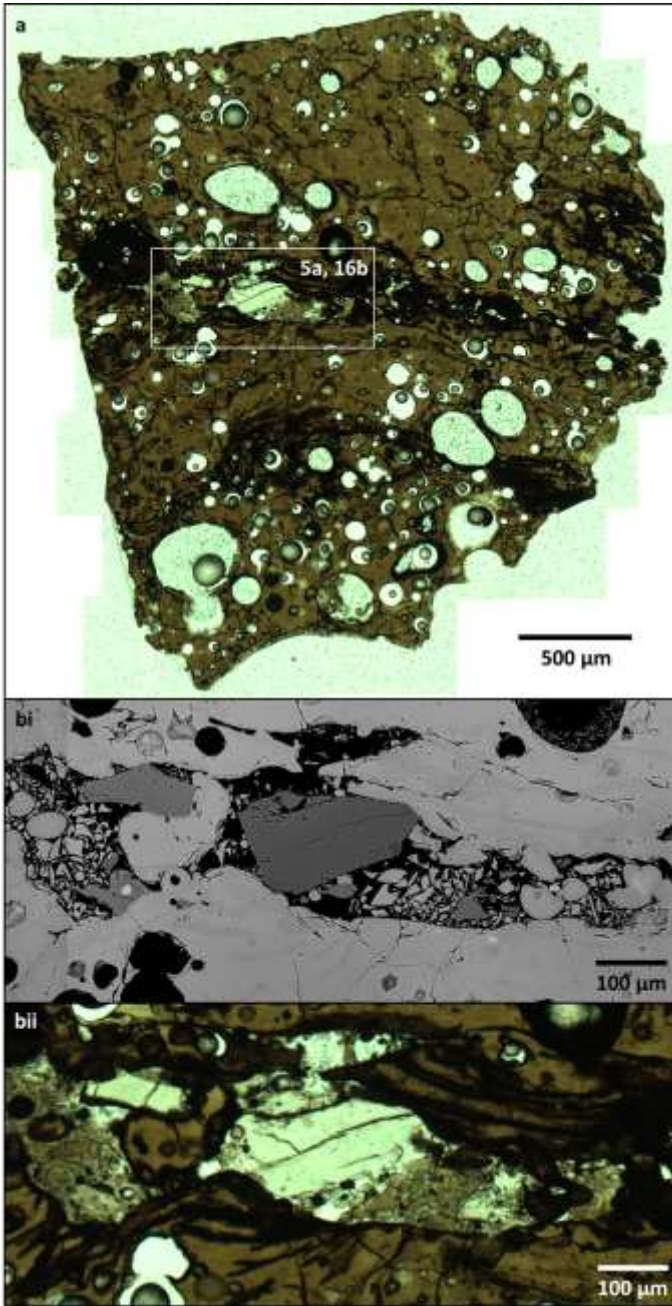
834 Thus we believe that the vast majority of the particles, fractures and connected bubbles seen in the
835 K1918 pyroclasts to be primary features indicative of the transportation of small particles of juvenile
836 and lithic material in a mobile fluid phase through a permeable network within the 1918 Katla magma.

837 4.11 How common are permeable gas and ash transporting pathways within basalt?

838 Although sintered particles within permeable pathways are common in rhyolite, they are thought to
839 be exclusive to silicic eruptions, yet particle sintering was found in 80% of the basaltic K1918 clasts
840 examined. There are three explanations for this absence from the literature: 1) the process that forms
841 them is extremely rare but there were some conditions specific to the K1918 eruption that allowed
842 them to be formed; 2) they are commonly created during basaltic eruptions but rarely preserved; near
843 simultaneous fragmentation and quenching during K1918 allowed this; 3) they are common features,
844 preserved readily in basaltic samples, but often overlooked, perhaps when observed, mistaken for bad
845 sample preparation.

846 We are inclined to think that the latter option is the most likely, based on the high abundance of
847 sintered/transported particles and permeable pathways within our samples (section 4.10). These
848 features are difficult to detect in conventional forms of observation (e.g. Fig. 4), requiring high
849 resolution analytical instruments (e.g. Field-emission microprobes or SEMs) for imaging and
850 compositional mapping. Most of the features were not obvious or else completely invisible in ppl (e.g.
851 Fig. 4a_{ii}).

852 Angular bubble-occupying particles are fairly common in natural volcanic samples, as are flowbands.
853 Careful image comparison has revealed that in the K1918 clasts, flow bands in ppl images tend to
854 represent microlite chains in BSE images (Figs. 7,10, 16), which in turn we infer to represent healed
855 void-spaces (e.g. Figs. 5,8,10,16). It therefore seems, at least in K1918 samples, that extensive flow-
856 banding represents (partially) healed fractures which may be filled with sintered particles (e.g. Fig.
857 16).



858

859 Figure 16: A clast bearing a particle filled sintered fracture which is inconspicuous in ppl, instead
860 appearing as an area of intensive flow-banding. (a) A ppl overview of jökulhlaup clast Mul 6 unit 3a-1

861 2,000-4,000 3a (~3 x 3 mm). The clast is predominantly sideromelane but has two dark horizontal
862 stripes of intensive flowbanding dissecting the sample; (b) Detail of the topmost dark stripe (see Figure
863 5a for a compositional map of the same area); (bi) a BSE image showing a partially healed fracture full
864 of sintered particles, surrounded by microlite chains; (bii) a ppl image of the same area showing flow
865 bands around a feature which is much less obviously a particle filled sintered fracture.

866 The features described in this paper are extremely widespread; evidence of particle sintering was
867 present in most clasts, with particularly good examples of fracture and bubble-filled particles present
868 in jökulhlaup samples. It would be scientifically useful to know whether such ash filled magmatic
869 fractures and bubbles exist in other basaltic magmas; and if so whether they are exclusive to subglacial
870 settings. Are they features which are actually common and have simply been overlooked, being merely
871 attributed to bad sample preparation and/or thought to show flowbanding? Or are they actually a
872 rare feature, uniquely preserved by the K1918 eruption?

873 5. Conclusions

874 We use textures and compositions to infer that fractures and connected bubbles acted as pathways
875 for gas and ash to be transported within a basaltic melt. Evidence appears primarily in the form of
876 angular to healed fractures, sintered ash particles, differing compositions between the ash particles
877 and host, apparent sorting of particles, S precipitation and a zone of low vesicularity surrounding a
878 partially healed fracture. Silicic particles and mineral fragments that belong to a more evolved melt
879 suggest that material was incorporated from the country rock, and that both juvenile and lithic
880 particles were transported through these systems, some of which have partly healed.

881 There are some similarities between these observed features and rhyolitic tuffisite veins. However, by
882 comparison, the pathways seem considerably smaller and more transient suggesting extremely rapid,
883 near simultaneous and successive episodes of brittle-ductile-brittle deformation. These observations
884 are significant, since it was previously thought that magmatic fractures and permeable gas/ash
885 networks only formed in high viscosity melts. The presence of such features at Katla could be
886 explained by rapid quenching which has allowed the preservation of such features.

887 This discovery challenges our conceptions of magma degassing, fluid and particle transport, and the
888 rheological properties of basaltic magma. In rhyolitic melts, tuffisite veins can cause a transition to
889 more effusive activity. The fractures within the Katla basalt do not appear to have significantly
890 degassed the magma as the clasts are still highly vesicular and erupted explosively. An alternative
891 explanation is that the fractures served to enhance explosivity by providing pathways by which
892 meltwater could infiltrate, enhancing both quenching and phreatomagmatic fragmentation. The
893 discovery of these fractures therefore could have important implications for our understanding of the
894 way in which basalt fragments.

895 We propose similar textures could be widespread in basaltic tephra from other settings but have
896 been largely ignored to date as dismissed as sample preparation artefacts. However, these textures
897 likely record key phases of magma damage, recycling and preparation for fuel coolant interactions.

898

899 6. Acknowledgements.

900 Jacqueline Owen is the beneficiary of a post-doctoral grant from the AXA Research Fund. Thomas
901 Shea and Hugh Tuffen were supported by a National Science Foundation grant EAR 1250366 and a
902 Royal Society University Research Fellowship respectively. Chris Hayward and Debbie Hurst assisted
903 greatly in lab analysis. Robert Duller, Lionel Wilson and Margherita Polacci contributed to fascinating
904 discussions as did a great number of people from the University of Iceland, including Magnús
905 Guðmundsson and William Moreland. We are grateful for the thoughtful and thorough edits
906 provided by Jérémie Vasseur and an anonymous reviewer. Final thanks go to James Gardner for
907 professional editing and insightful comments.

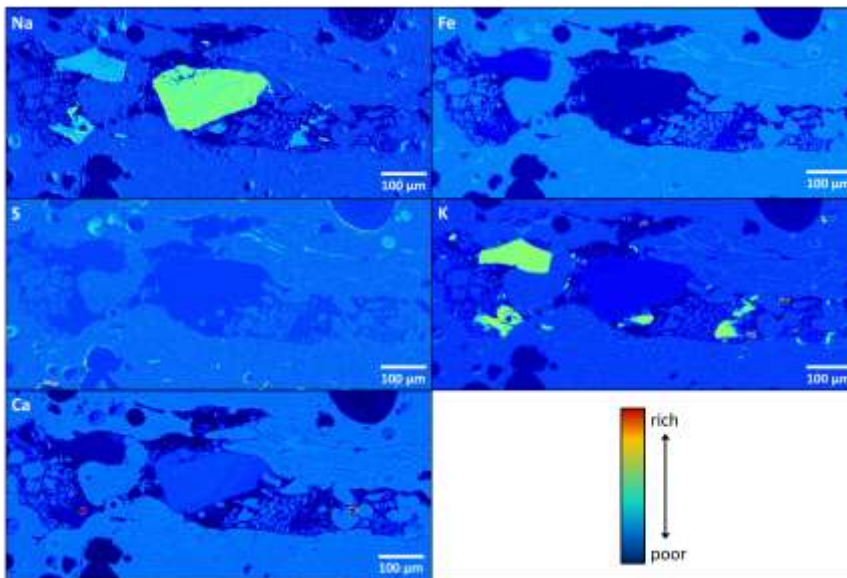
908

909 APPENDIX

910 Appendix 1: Compositional maps

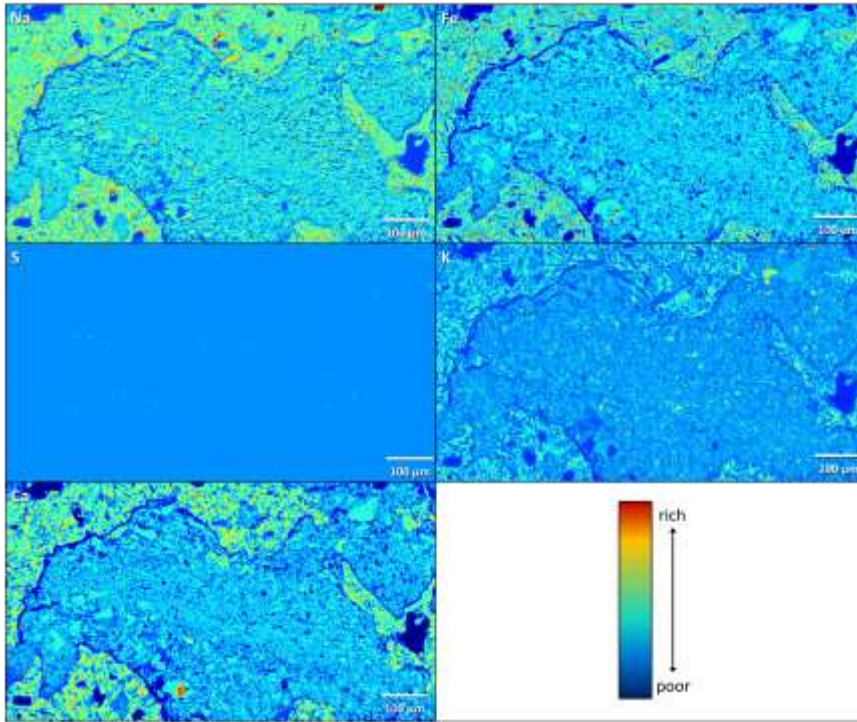
911 As described in the methods, EPMA was used to make compositional (x-ray distribution) maps. Five
912 spectrometers were used to measure the relative abundance of S, Ca, Fe, K and either Na or F. The
913 data was used to make single 2D intensity matrices as shown in Figures A1, A2 and A3. These images
914 were then combined to create the RGB composite image shown in Figure 5. The relative abundance
915 of all five elements was considered when making compositional interpretations as described in the
916 text.

917



918

919 A1: 2D single intensity matrices for the fracture shown in Figure 5a. Each image represents the
920 relative abundance of a single element (Na, Fe, S, K or Ca) as indicated by the chemical symbol in the
921 top left corner of each image. Hot and cold colours represent high and low abundances respectively.

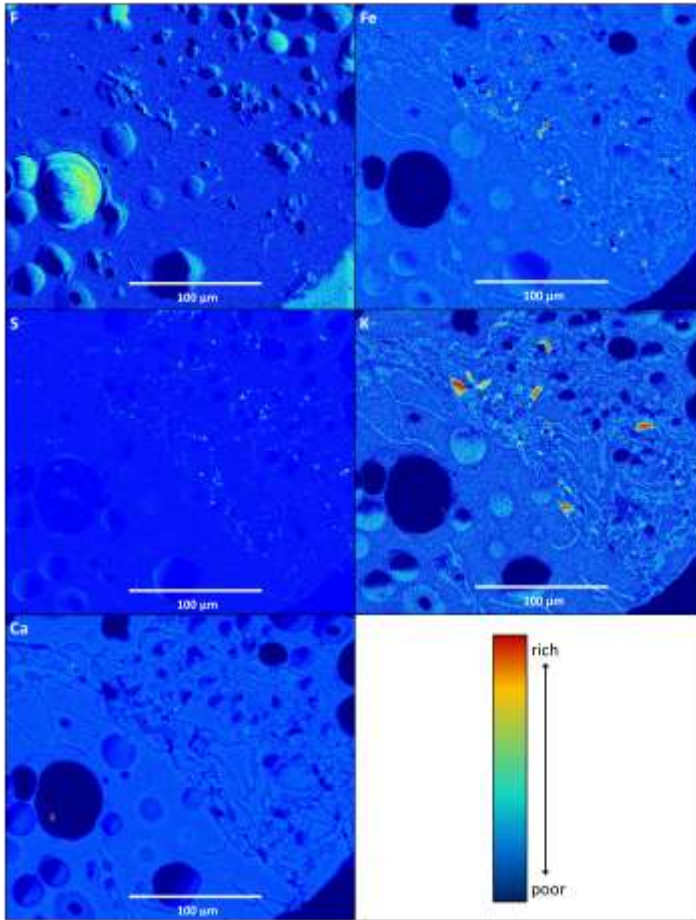


922

923

924 Figure A2: 2D single intensity matrices for the particle filled bubble shown in Figure 5b. Each image
 925 represents the relative abundance of a single element (Na, Fe, S, K or Ca) as indicated by the
 926 chemical symbol in the top left corner of each image. Cold and hot colours represent low and high
 927 abundances respectively.

928



929

930 Figure A3: 2D single intensity matrices for the area of intensive microlite chains shown in Figure 5c.
 931 Each image represents the relative abundance of a single element (F, Fe, S, K or Ca) as indicated by
 932 the chemical symbol in the top left corner of each image. Cold and hot colours represent low and
 933 high abundances respectively.

934 Appendix 2: Thermal calculations to estimate sintering timescales

935

936 To estimate sintering timescales we assume a three step process: (1) thermal equilibration, (2) clast
 937 rounding, (3) welding to 'healed' state.

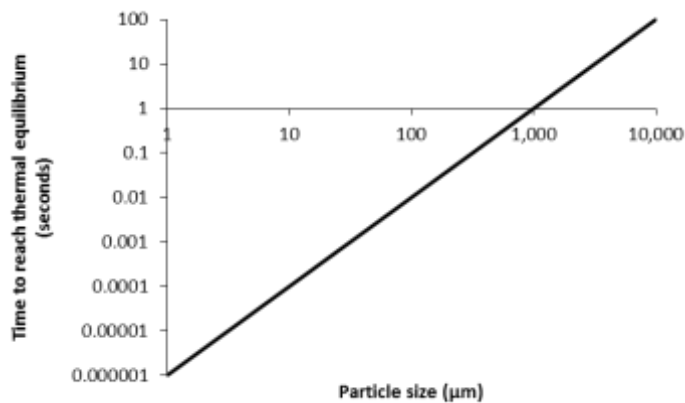
938 The fact that so many of the particles are angular, suggests brittle fragmentation and therefore that
 939 the magma was below T_g . Furthermore, we hypothesise that the more evolved particles represent
 940 older silicic Katla material, which was incorporated into permeable pathways during magma ascent,
 941 and therefore presumably entered the system at temperatures closer to ambient. Therefore, for

942 these particles to sinter, the first step will be for them to gain magmatic temperature i.e. reach
943 thermal equilibrium. The timescale for thermal equilibrium to be reached (t_{eq} in s) can be estimated
944 using this equation (Wilson and Mougini-Mark, 2003)

$$t_{eq} \sim \frac{r^2}{\kappa} \quad (3)$$

947 where r is particle radius (in m) and κ is thermal diffusivity (in $\text{m}^2 \text{s}^{-1}$). Thermal diffusivity varies (0.5 -
948 $2.0 \times 10^{-6} \text{ m}^2 \text{ s}^{-1}$) as a function of temperature and to a lesser effect composition (Vosteen and
949 Schellschmidt, 2003; Whittington et al., 2009; Eppelbaum et al., 2014), however, in the interests of
950 simplicity we will take an ~average value of $1 \times 10^{-6} \text{ m}^2 \text{ s}^{-1}$ which is considered the general thermal
951 diffusivity for all silicates (Wilson and Mougini-Mark, 2003)

952



953

954 Figure A4: Expected times for particles to meet thermal equilibrium as a function of particle size

955 Typical intra void particles are $<100 \mu\text{m}$ and therefore would have reached thermal equilibrium in a
956 matter of milliseconds (Fig. A4). We therefore, deem this process insignificant in effecting the
957 timescale of sintering.

958 Many papers discuss the timescales of sintering e.g. (e.g. Uhlmann et al., 1975; Ristić and Milosević,
959 2006; Pope, 2015), however, these models assume that the starting media consists of spherical
960 particles. Natural ash particles are not spherical. It seems from our samples that some of the ash
961 particles have experienced rounding, whereas others have not, therefore, it would be interesting to
962 estimate the timescale of this rounding/relaxation process that occurs prior to sintering. We are only
963 aware of one study (Pope, 2015) that has tried to estimate rounding rates of natural samples
964 however, this was performed on rhyolitic particles from Cordon Caulle, Chile, and no general
965 relationships were observed between rounding rate, grain size and temperature. We therefore
966 turned to the equation used to estimate the rounding rate of vesicles within magma (Gardner et al.,
967 2017):

968

$$\lambda = \frac{\eta r}{\sigma}$$

969

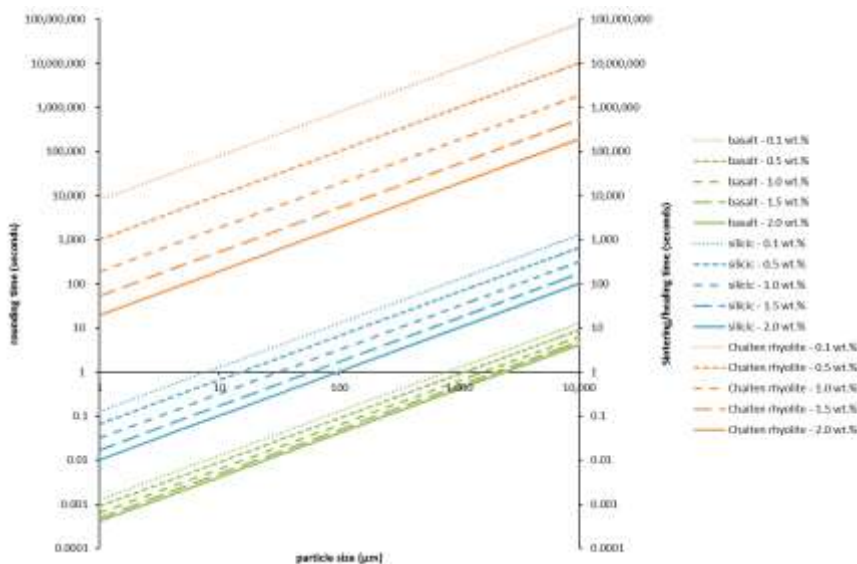
(4)

970 where λ is the relaxation time (in s) that a non-spherical bubble will take to relax into a spherical
 971 form, η is melt viscosity (in Pa s), r is particle radius (in m) and σ is melt surface tension (in N m⁻¹).
 972 When this equation was applied to the parameters of the particles used by Pope (2015) the
 973 calculated relaxation time was very similar to the timescales of clast rounding observed in their
 974 experiments. Therefore, we will use equation (4) as a proxy for the relaxation/rounding rate of Katla
 975 clasts.

976 Viscosities were estimated using the model of Giordano et al. (2008) our EPMA data and the
 977 assumption that the magma was 1045 °C. We also modelled typical rhyolite from Chaitén at 800 °C
 978 (Castro and Dingwell, 2009), where tuffsite veins and sintering are common (Castro et al., 2012;
 979 Berlo et al., 2013; Saubin et al., 2016). Although surface tension (σ) varies as a function of various
 980 magmatic parameters (Bagdassarov et al., 2000; Mangan and Sisson, 2005; Gardner and Ketcham,
 981 2011; Gardner et al., 2013), H₂O content is the only parameter considered to have a significant
 982 effect, with melt composition and temperature only playing a very minor role (Walker and Mullins,
 983 1981; Bagdassarov et al., 2000; Gardner et al., 2013; Gardner et al., 2017). We therefore chose a
 984 single value of 0.3 N m⁻¹ for all modelling which is consistent with literature values for relatively dry
 985 silicate melts (Taniguchi, 1988; Phillips et al., 1995; Gardner and Denis, 2004; Sumner et al., 2005).

986

987



988

989 Figure A5: expected times for particles to round/sinter as a function of particle size and dissolved
990 H₂O content (0.1 -2.0 wt.% as shown in the legend). Note that the rounding timescale and
991 sinetering/healing timescale were calculated in the same way and therefore have the same value.
992 Therefore, the combined rounding and sintering rate can be found by simply doubling the values in
993 this figure. Green and blue lines refer to samples within this study at an assumed temperature of
994 1045 °C. The orange lines model Chaiten rhyolite at 800 °C (using composition data from Castro and
995 Dingwell (2009)) where tuffisite veins are often found.

996

997 Once connections are made between particles, the pore spaces can ‘heal’ through viscous flow
998 (Ristić and Milosević, 2006; Vasseur et al., 2013). The following equation can be used to estimate the
999 timescale τ_s of viscous sintering (Vasseur et al., 2013)

1000

$$\tau_{s=} \frac{R_i \eta}{\gamma}$$

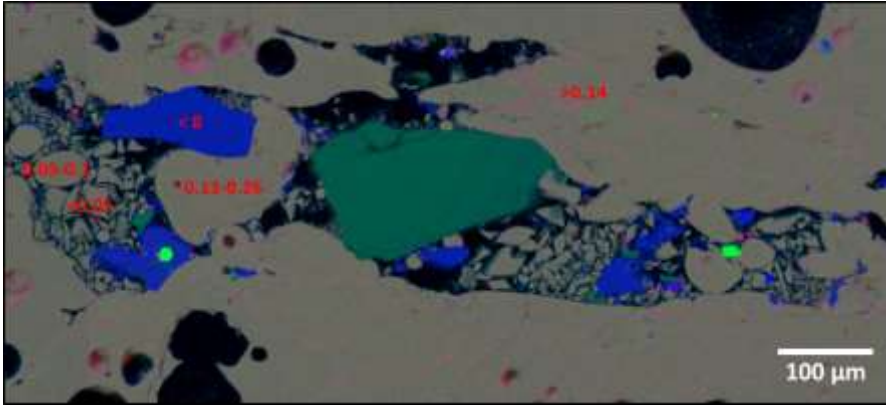
1001

(5)

1002 where R_i is the initial radius, η is melt viscosity and γ is the melt-vapour interfacial tension. Note that
1003 this is essentially the same equation as that for the viscous relaxation of bubbles (Vasseur et al.,
1004 2013). As we are using the latter to estimate the rounding rate of the particles, and because we
1005 disregard the timescales for thermal equilibrium as being insignificantly small, then our combined
1006 timescale for the complete sintering of the sub millimetric 1918 A.D. Katla particles to become
1007 healed glass can be estimated by doubling equation (4) or (5) and thus the values in Figure A5.

1008 Typically, inter-void particles are approximately $\leq 100 \mu\text{m}$ in diameter. For basaltic particles with 0.2-
1009 0.3 wt.% H₂O (as measured with FTIR) this equates to rounding times of ≤ 0.1 seconds, and thus full
1010 healing times of approximately ≤ 0.2 seconds. These resultant times, are perhaps a little
1011 unrealistically short. However, they give an idea of relative differences between particles e.g. it can
1012 be seen that silicic particles of the same size will take considerably longer to sinter (Figs. A5, A6).
1013 Furthermore, even if the absolute values were out by a few orders of magnitude (it is difficult to
1014 suggest reasons for errors larger than this), then it still equates to extremely short residence times
1015 for the permeable networks and times much shorter than for Chaitén rhyolite at 800 °C (Fig. A5)
1016 (Castro et al., 2012) where our estimated values closely match observations (Pope, 2015). Thus we
1017 can be confident that our estimates are reasonable ball park amounts.

1018



1019

1020 Figure A6: The compositional map from Figure 5a, with estimated residence times (in seconds),
 1021 assuming low H₂O concentrations (consistent with observations) shown in red.

1022 The thermal estimations can help explain some of the particle morphologies as well as shed insights
 1023 into timescales. For example, our calculations suggest the large rounded basaltic particle in Figure
 1024 A6, had to be hot for at least 0.13 seconds to be deformable, however if it had been at 1045 °C
 1025 for more than 0.26 seconds it would have completely annealed with the surrounding melt. The
 1026 angular silicic particle (blue) next to it required ~8 seconds at 1045 °C to relax into a sphere. The fact
 1027 that it has not rounded, therefore suggests a residence time < 8 seconds. The smaller rounded
 1028 basaltic particles require residence times of 0.05-0.1 seconds, whilst the angular clasts must have
 1029 been resident for <0.05 seconds. If we assume that the microlite chains (in pink above the fracture)
 1030 represent the former boundaries of annealed particles then using their approximate dimensions,
 1031 these particles must have been present for more than >0.14 seconds to anneal together. All of this is
 1032 consistent with a fracture opening for a fraction of a second, and having a momentary stream of
 1033 particles before quenching. However, it is impossible to tell the extent of the annealed particles
 1034 beyond the pink microlites (presumably prolonged heating will completely homogenise the melt),
 1035 therefore a more conservative estimate for the lifetime of each permeable network would be on the
 1036 order of a second or so.

1037 We estimate that the fracture in Figure 5a was open for a slightly longer duration than the
 1038 connected bubbles in Figure 5b where nearly all of the particles are incredibly small (~5 μm) and
 1039 angular. Our thermal calculations suggest that these particles could not have been resident for > 0.05
 1040 seconds suggesting a near instantaneous injection and quenching process.

1041 For Figure 5c, we estimate that the network was permeable for ~ 0.05-0.4 seconds. The first number
 1042 represents the time taken to completely sinter and heal basalt, and the latter is the time required to
 1043 round dacite; both assuming a particle size of ~5 μm which seems to be the approximate average
 1044 size of the remaining silicic particles.

1045

1046 Appendix 3 - Diffusion estimates

1047 Bubble-poor zones next to voids can be interpreted to show areas of diffusive volatile loss into the
1048 void-space (Saubin et al., 2016; Webb et al., 2017). The void in Figure 4b shows a clear zone of bubble-
1049 poor glass extending approximately equidistant from the void wall. The average width of the bubble-
1050 poor zone is ~80 μm , which can be inferred to represent the volatile diffusion distance. The fact that
1051 these fractures have been preserved, suggests that they formed at a relatively shallow level in the
1052 conduit, thus it is likely that H_2O will be the predominant species that is diffusing. The diffusivity of
1053 H_2O (D) in m^2s^{-1} for a basaltic melt of 0.2 wt.% H_2O (a reasonable assumption given the measured FTIR
1054 concentrations, and assuming our interpretation of shallow level is correct) can be expressed with
1055 the following equation from Zhang and Stolper (1991):

$$\ln D = -(12.49 \pm 2.35) - (15200 \pm 3900)/T \quad (6)$$

1058 where T is temperature in Kelvin, inferred to be 1318 K (1045 $^\circ\text{C}$) based on our oxide thermometry
1059 results. Assuming that the opening of a fracture results in disequilibrium within the melt, the H_2O
1060 diffusion distance (L) in m, is roughly approximated by the following equation from Zhang and Stolper
1061 (1991):

$$L \cong 2\sqrt{Dt} \quad (7)$$

1064 where t is time in seconds. Combining equations (6) and (7), we obtain a diffusion time of ~40s for H_2O
1065 to diffuse ~80 μm into the fracture.

1066

1067 References

- 1068 Adams, N.K., Houghton, B.F., Fagents, S.A. and Hildreth, W., 2006. The transition from explosive to
1069 effusive eruptive regime: The example of the 1912 Novarupta eruption, Alaska. Geological
1070 Society of America Bulletin, 118(5-6): 620-634. 10.1130/b25768.1
- 1071 Allard, P., 2010. A CO_2 -rich gas trigger of explosive paroxysms at Stromboli basaltic volcano, Italy.
1072 Journal of Volcanology and Geothermal Research, 189(3-4): 363-374.
1073 <http://dx.doi.org/10.1016/j.jvolgeores.2009.11.018>
- 1074 Anderson, S.W. and Fink, J.H., 1989. Hydrogen-Isotope Evidence for Extrusion Mechanisms of the
1075 Mount-St-Helens Lava Dome. Nature, 341(6242): 521-523. 10.1038/341521a0
- 1076 Anderson, S.W., Fink, J.H. and Rose, W.I., 1995. Mount St Helens and Santiaguito lava domes: The
1077 effect of short-term eruption rate on surface texture and degassing processes. Journal of
1078 Volcanology and Geothermal Research, 69(1-2): 105-116. [https://doi.org/10.1016/0377-0273\(95\)00022-4](https://doi.org/10.1016/0377-0273(95)00022-4)
- 1079
- 1080 Bacon, C.R. and Hirschmann, M.M., 1988. Mg/Mn partitioning as a test for equilibrium between
1081 coexisting Fe-Ti oxides. Am. Mineral., 73: 57-61. 0003-004x/88/0102-o057
- 1082 Bagdassarov, N., Dorfman, A. and Dingwell, D.B., 2000. Effect of alkalis, phosphorus, and water on
1083 the surface tension of haplogranite melt. Am Mineral, 85(1): 33-40.
1084 <https://doi.org/10.2138/am-2000-0105>
- 1085 Berlo, K., Tuffen, H., Smith, V.C., Castro, J.M., Pyle, D.M., Mather, T.A. and Geraki, K., 2013. Element
1086 variations in rhyolitic magma resulting from gas transport. Geochimica et Cosmochimica
1087 Acta, 121: 436-451. <http://dx.doi.org/10.1016/j.gca.2013.07.032>

1088 Blundy, J. and Cashman, K., 2008. Petrologic reconstruction of magmatic system variables and
1089 processes. *Minerals, Inclusions and Volcanic Processes*, 69(1): 179-239.
1090 <https://doi.org/10.2138/rmg.2008.69.6>

1091 Blundy, J., Cashman, K. and Humphreys, M., 2006. Magma heating by decompression-driven
1092 crystallization beneath andesite volcanoes. *Nature*, 443(7107): 76-80. 10.1038/nature05100

1093 Bottinga, Y. and Weill, D.F., 1970. Densities of liquid silicate systems calculated from partial molar
1094 volumes of oxide components. *Am J Sci*, 269(2): 169-182. 10.2475/ajs.269.2.169

1095 Budd, D.A., Troll, V.R., Dahren, B. and Burchardt, S., 2016. Persistent multitiered magma plumbing
1096 beneath Katla volcano, Iceland. *Geochemistry, Geophysics, Geosystems*, 17(3): 966-980.
1097 10.1002/2015GC006118

1098 Castro, J.M., Cordonnier, B., Tuffen, H., Tobin, M., Puskar, L., Martin, M.C. and Bechtel, B., 2012. The
1099 role of melt-fracture degassing in defusing explosive rhyolite eruptions at volcán Chaitén.
1100 *Earth and Planetary Science Letters*, 333-334: 63-69.
1101 <https://doi.org/10.1016/j.epsl.2012.04.024>

1102 Castro, J.M. and Dingwell, D.B., 2009. Rapid ascent of rhyolitic magma at Chaiten volcano, Chile.
1103 *Nature*, 461(7265): 780-U729. 10.1038/nature08458

1104 Denton, J.S., Tuffen, H., Gilbert, J.S. and Odling, N., 2009. The hydration and alteration of perlite and
1105 rhyolite. *J Geol Soc London*, 166: 895-904. 10.1144/0016-76492008-007

1106 Dixon, J.E., Stolper, E. and Delaney, J.R., 1988. Infrared Spectroscopic Measurements of Co₂ and H₂O
1107 in Juan-De-Fuca Ridge Basaltic Glasses. *Earth and Planetary Science Letters*, 90(1): 87-104.
1108 [https://doi.org/10.1016/0012-821X\(88\)90114-8](https://doi.org/10.1016/0012-821X(88)90114-8)

1109 Duller, R.A., Mountney, N.P., Russell, A.J. and Cassidy, N.C., 2008. Architectural analysis of a
1110 volcanoclastic jökulhlaup deposit, southern Iceland: sedimentary evidence for supercritical
1111 flow. *Sedimentology*, 55(4): 939-964. 10.1111/j.1365-3091.2007.00931.x

1112 Edmonds, M. and Gerlach, T.M., 2007. Vapor segregation and loss in basaltic melts. *Geology*, 35(8):
1113 751-754. 10.1130/g23464a.1

1114 Eichelberger, J.C., Carrigan, C.R., Westrich, H.R. and Price, R.H., 1986. Non-explosive silicic volcanism.
1115 *Nature*, 323(6089): 598-602. 10.1038/323598a0

1116 Eppelbaum, L., Kutasov, I. and Pilchin, A., 2014. *Thermal Properties of Rocks and Density of Fluids,*
1117 *Applied Geothermics.* Springer-Verlag, Berlin Heidelberg. 10.1007/978-3-642-34023-9_2

1118 Farquharson, J.I., Wadsworth, F.B., Heap, M.J. and Baud, P., 2017. Time-dependent permeability
1119 evolution in compacting volcanic fracture systems and implications for gas overpressure.
1120 *Journal of Volcanology and Geothermal Research*, 339: 81-97.
1121 <https://doi.org/10.1016/j.jvolgeores.2017.04.025>

1122 Gardner, J.E. and Denis, M.-H., 2004. Heterogeneous bubble nucleation on Fe-Ti oxide crystals in
1123 high-silica rhyolitic melts1. *Geochimica et Cosmochimica Acta*, 68(17): 3587-3597.
1124 <http://doi.org/10.1016/j.gca.2004.02.021>

1125 Gardner, J.E. and Ketcham, R.A., 2011. Bubble nucleation in rhyolite and dacite melts: temperature
1126 dependence of surface tension. *Contrib Mineral Petr*, 162(5): 929-943. 10.1007/s00410-011-
1127 0632-5

1128 Gardner, J.E., Ketcham, R.A. and Moore, G., 2013. Surface tension of hydrous silicate melts:
1129 Constraints on the impact of melt composition. *Journal of Volcanology and Geothermal*
1130 *Research*, 267: 68-74. <http://doi.org/10.1016/j.jvolgeores.2013.09.007>

1131 Gardner, J.E., Llewellyn, E.W., Watkins, J.M. and Befus, K.S., 2017. Formation of obsidian pyroclasts
1132 by sintering of ash particles in the volcanic conduit. *Earth and Planetary Science Letters*, 459:
1133 252-263. <http://doi.org/10.1016/j.epsl.2016.11.037>

1134 Gaunt, H.E., Sammonds, P.R., Meredith, P.G., Smith, R. and Pallister, J.S., 2014. Pathways for
1135 degassing during the lava dome eruption of Mount St. Helens 2004–2008. *Geology*, 42(11):
1136 947-950. 10.1130/g35940.1

1137 Ghiorso, M.S. and Evans, B.W., 2008. Thermodynamics of rhombohedral oxide solid solutions and a
1138 revision of the Fe-Ti two-oxide geothermometer and oxygen-barometer. *Am. J. Sci.*, 308:
1139 957-1039. 10.2475/09.2008.01

1140 Giordano, D. and Dingwell, D.B., 2003. Viscosity of hydrous Etna basalt: implications for Plinian-style
1141 basaltic eruptions. *Bulletin of Volcanology*, 65(1): 8-14. 10.1007/s00445-002-0233-2

1142 Giordano, D., Russell, J.K. and Dingwell, D.B., 2008. Viscosity of magmatic liquids: A model. *Earth and
1143 Planetary Science Letters*, 271(1-4): 123-134. 10.1016/j.epsl.2008.03.038

1144 Gonnermann, H.M. and Manga, M., 2005. Nonequilibrium magma degassing: Results from modeling
1145 of the ca. 1340 A.D. eruption of Mono Craters, California. *Earth and Planetary Science
1146 Letters*, 238(1-2): 1-16. 10.1016/j.epsl.2005.07.021

1147 Gudmundsson, M.T., 2013. Melting of Ice by Magma-Ice-Water Interactions During Subglacial
1148 Eruptions as an Indicator of Heat Transfer in Subaqueous Eruptions, Explosive Subaqueous
1149 Volcanism. *American Geophysical Union*, pp. 61-72. 10.1029/140GM04

1150 Gudmundsson, M.T., Sigmundsson, F. and Bjornsson, H., 1997. Ice-volcano interaction of the 1996
1151 Gjalp subglacial eruption, Vatnajökull, Iceland. *Nature*, 389(6654): 954-957. 10.1038/40122

1152 Hayward, C., 2011. High spatial resolution electron probe microanalysis of tephra and melt
1153 inclusions without beam-induced chemical modification. *The Holocene*, 22(1): 119-125.
1154 10.1177/0959683611409777

1155 Hoblitt, R.P. and Harmon, R.S., 1993. Bimodal density distribution of cryptodome dacite from the
1156 1980 eruption of Mount St. Helens, Washington. *Bulletin of Volcanology*, 55: 421-437.
1157 <https://doi.org/10.1007/BF00302002>

1158 Hoskuldsson, A. and Sparks, R.S.J., 1997. Thermodynamics and fluid dynamics of effusive subglacial
1159 eruptions. *Bulletin of Volcanology*, 59(3): 219-230. <https://doi.org/10.1007/s004450050187>

1160 Houghton, B.F. and Gonnermann, H.M., 2008. Basaltic explosive volcanism: Constraints from
1161 deposits and models. *Chemie der Erde - Geochemistry*, 68(2): 117-140.
1162 10.1016/j.chemer.2008.04.002

1163 Humphreys, M.C.S., Edmonds, M., Christopher, T. and Hards, V., 2009. Chlorine variations in the
1164 magma of Soufrière Hills Volcano, Montserrat: Insights from Cl in hornblende and melt
1165 inclusions. *Geochimica et Cosmochimica Acta*, 73(19): 5693-5708.
1166 10.1016/j.gca.2009.06.014

1167 Jaupart, C., 1998. Gas loss from magmas through conduit walls during eruption. In: J.S. Gilbert and
1168 R.S.J. Sparks (Editors), *The physics of explosive volcanic eruptions*. Geological Society Special
1169 Publication, No. 145, 73-90. 10.1144/gsl.sp.1996.145.01.05

1170 Jaupart, C. and Allègre, C.J., 1991. Gas content, eruption rate and instabilities of eruption regime in
1171 silicic volcanoes. *Earth and Planetary Science Letters*, 102(3-4): 413-429. 10.1016/0012-
1172 821x(91)90032-d

1173 Jóhannesson, H. and Sæmundsson, K., 2014. Geological map of Iceland. *Bedrock Geology*.1: 600,000.
1174 Icelandic Institute of Natural History.

1175 Kendrick, J.E., Lavallée, Y., Varley, N., Wadsworth, F.B., Lamb, O.D. and Vasseur, J., 2016. Blowing off
1176 steam: Tuffisite formation as a regulator for lava dome eruptions. *Frontiers in Earth Science*,
1177 4. 10.3389/feart.2016.00041

1178 Klug, C. and Cashman, K.V., 1996. Permeability development in vesiculating magmas: implications for
1179 fragmentation. *Bulletin of Volcanology*, 58(2): 87-100. 10.1007/s004450050128

1180 Kolzenburg, S., Heap, M.J., Lavallée, Y., Russell, J.K., Meredith, P.G. and Dingwell, D.B., 2012.
1181 Strength and permeability recovery of tuffisite-bearing andesite. *Solid Earth*, 3(2): 191-198.
1182 10.5194/se-3-191-2012

1183 Lacasse, C., Sigurdsson, H., Carey, S.N., Jóhannesson, H., Thomas, L.E. and Rogers, N.W., 2007.
1184 Bimodal volcanism at the Katla subglacial caldera, Iceland: insight into the geochemistry and
1185 petrogenesis of rhyolitic magmas. *Bulletin of Volcanology*, 69(4): 373-399. 10.1007/s00445-
1186 006-0082-5

1187 Lacasse, C., Sigurdsson, H., Jóhannesson, H., Paterne, M. and Carey, S., 1995. Source of Ash Zone 1 in
1188 the North Atlantic. *Bulletin of Volcanology*, 57(1): 18-32. [10.1007/bf00298704](https://doi.org/10.1007/bf00298704)
1189 Larsen, G., 2000. Holocene eruptions within the Katla volcanic system, south Iceland: Characteristics
1190 and environmental impact. *Jökull*, 49: 1-28.
1191 Larsen, G., 2010. 3 Katla: Tephrochronology and Eruption History. In: J.K. Anders Schomacker and
1192 H.K. Kurt (Editors), *Developments in Quaternary Science*. Elsevier, pp. 23-49. [10.1016/s1571-](https://doi.org/10.1016/s1571-0866(09)01303-7)
1193 [0866\(09\)01303-7](https://doi.org/10.1016/s1571-0866(09)01303-7)
1194 Larsen, G., Eiriksson, J. and Gudmundsdóttir, E.R., 2014. Last millennium dispersal of air-fall tephra
1195 and ocean-rafted pumice towards the north Icelandic shelf and the Nordic seas. *Geological*
1196 *Society, London, Special Publications*, 398(1): 113-140. [10.1144/sp398.4](https://doi.org/10.1144/sp398.4)
1197 Larsen, G., Newton, A.J., Dugmore, A.J. and Vilmundardóttir, E.G., 2001. Geochemistry, dispersal,
1198 volumes and chronology of Holocene silicic tephra layers from the Katla volcanic system,
1199 Iceland. *J Quaternary Sci*, 16(2): 119-132. [10.1002/jqs.587](https://doi.org/10.1002/jqs.587)
1200 Maizels, J., 1992. Boulder Ring Structures Produced during Jökulhlaup Flows. Origin and Hydraulic
1201 Significance. *Geografiska Annaler. Series A, Physical Geography*, 74(1): 21-33.
1202 [10.2307/521467](https://doi.org/10.2307/521467)
1203 Maizels, J., 1993. Lithofacies variations within sandur deposits: the role of runoff regime, flow
1204 dynamics and sediment supply characteristics. *Sediment Geol*, 85(1): 299-325.
1205 [https://doi.org/10.1016/0037-0738\(93\)90090-R](https://doi.org/10.1016/0037-0738(93)90090-R)
1206 Mangan, M. and Sisson, T., 2005. Evolution of melt-vapor surface tension in silicic volcanic systems:
1207 Experiments with hydrous melts. *Journal of Geophysical Research: Solid Earth*, 110(B1): n/a-
1208 n/a. [10.1029/2004JB003215](https://doi.org/10.1029/2004JB003215)
1209 Martel, C., Pichavant, M., Bourdier, J.L., Traineau, H., Holtz, F. and Scaillet, B., 1998. Magma storage
1210 conditions and control of eruption regime in silicic volcanoes: experimental evidence from
1211 Mt. Pelée. *Earth and Planetary Science Letters*, 156(1-2): 89-99. [10.1016/s0012-](https://doi.org/10.1016/s0012-821x(98)00003-x)
1212 [821x\(98\)00003-x](https://doi.org/10.1016/s0012-821x(98)00003-x)
1213 Menand, T. and Phillips, J.C., 2007. Gas segregation in dykes and sills. *Journal of Volcanology and*
1214 *Geothermal Research*, 159(4): 393-408. <http://dx.doi.org/10.1016/j.jvolgeores.2006.08.003>
1215 Moore, G., Vennemann, T. and Carmichael, I.S.E., 1998. An empirical model for the solubility of H₂O
1216 in magmas to 3 kilobars. *Am Mineral*, 83(1-2): 36-42. [https://doi.org/10.2138/am-1998-1-](https://doi.org/10.2138/am-1998-1-203)
1217 [203](https://doi.org/10.2138/am-1998-1-203)
1218 Morrissey, M., Zimanowski, B., Wohletz, K. and Buettner, R., 2000. Phreatomagmatic fragmentation.
1219 In: H. Sigurdsson (Editor), *Encyclopedia of Volcanoes*. Academic Press, San Diego, pp. 431-
1220 445.
1221 Nakada, S., Uto, K., Sakuma, S., Eichelberger, J. and Shimizu, H., 2005. Scientific Results of Conduit
1222 Drilling in the Unzen Scientific Drilling Project (USDP). *Scientific Drilling*, 1: 18-22.
1223 <http://doi.org/10.2204/iodp.sd.1.03.2005>
1224 Namiki, A. and Manga, M., 2008. Transition between fragmentation and permeable outgassing of
1225 low viscosity magmas. *Journal of Volcanology and Geothermal Research*, 169(1-2): 48-60.
1226 <http://dx.doi.org/10.1016/j.jvolgeores.2007.07.020>
1227 Newman, S. and Lowenstern, J.B., 2002. VolatileCalc: a silicate melt-H₂O-CO₂ solution model
1228 written in Visual Basic for excel. *Computers & Geosciences*, 28(5): 597-604. [10.1016/s0098-](https://doi.org/10.1016/s0098-3004(01)00081-4)
1229 [3004\(01\)00081-4](https://doi.org/10.1016/s0098-3004(01)00081-4)
1230 Newton, A., 1999. Ocean-transported pumice in the North Atlantic. PhD thesis Thesis, University of
1231 Edinburgh.
1232 Noguchi, S., Toramaru, A. and Nakada, S., 2008. Groundmass crystallization in dacite dykes taken in
1233 Unzen Scientific Drilling Project (USDP-4). *Journal of Volcanology and Geothermal Research*,
1234 175(1-2): 71-81. <http://dx.doi.org/10.1016/j.jvolgeores.2008.03.037>
1235 O'Connor, J.E. and Costa, J.E., 2004. The world's largest floods, past and present: their causes and
1236 magnitudes. U.S. Geological Survey, University of Minnesota.

1237 Óladóttir, B., Sigmarsson, O., Larsen, G. and Thordarson, T., 2008. Katla volcano, Iceland: magma
1238 composition, dynamics and eruption frequency as recorded by Holocene tephra layers.
1239 *Bulletin of Volcanology*, 70(4): 475-493. 10.1007/s00445-007-0150-5
1240 Óladóttir, B.A., Larsen, G., Þórðarson, Þ. and Sigmarsson, O., 2005. The Katla volcano S-Iceland:
1241 Holocene tephra stratigraphy and eruption frequency. *Jökull*, 55: 53-74.
1242 Owen, J., 2016. Using volatiles in magma to decipher subglacial eruption dynamics. *Geology Today*,
1243 32(1): 30-37. 10.1111/gto.12127
1244 Owen, J., Shea, T. and Tuffen, H., 2017. The role of bubbles during the 1918 subglacial basalt
1245 eruption of Katla, south Iceland., Joint Assembly TSG-VMSG-BGA, University of Liverpool, pp.
1246 163.
1247 Owen, J., Tuffen, H. and McGarvie, D., in press. Magma degassing in the effusive-explosive subglacial
1248 rhyolitic eruption of Dalakvísl, Torfajökull, Iceland: insights into quenching pressures, palaeo-
1249 ice thickness, and edifice erosion. *Jökull*.
1250 Owen, J., Tuffen, H. and McGarvie, D.W., 2012. Using dissolved H₂O in rhyolitic glasses to estimate
1251 palaeo-ice thickness during a subglacial eruption at Bláhnúkur (Torfajökull, Iceland). *Bulletin*
1252 *of Volcanology*, 74(6): 1355-1378. 10.1007/s00445-012-0601-5
1253 Owen, J., Tuffen, H. and McGarvie, D.W., 2013a. Explosive subglacial rhyolitic eruptions in Iceland
1254 are fuelled by high magmatic H₂O and closed-system degassing. *Geology*, 41(2): 251-254.
1255 10.1130/G33647.1
1256 Owen, J., Tuffen, H. and McGarvie, D.W., 2013b. Pre-eruptive volatile content, degassing paths and
1257 depressurisation explaining the transition in style at the subglacial rhyolitic eruption of
1258 Dalakvísl, South Iceland. *Journal of Volcanology and Geothermal Research*, 258: 143–162.
1259 <https://doi.org/10.1016/j.jvolgeores.2013.03.021>
1260 Papale, P., 1999. Strain-induced magma fragmentation in explosive eruptions. *Nature*, 397: 425-428.
1261 10.1038/17109
1262 Phillips, J.C., Lane, S.J., Lejeune, A.-M. and Hilton, M., 1995. Gum rosin-acetone system as an
1263 analogue to the degassing behaviour of hydrated magmas. *Bulletin of Volcanology*, 57(4):
1264 263-268. 10.1007/bf00265425
1265 Plail, M., Edmonds, M., Humphreys, M.C.S., Barclay, J. and Herd, R.A., 2014. Geochemical evidence
1266 for relict degassing pathways preserved in andesite. *Earth and Planetary Science Letters*,
1267 386: 21-33. <http://dx.doi.org/10.1016/j.epsl.2013.10.044>
1268 Pope, R., 2015. Sintering of fragmented rhyolitic magma in the Cordón Caulle vent, Chile. MSc thesis
1269 Thesis, Lancaster University.
1270 Proussevitch, A.A. and Sahagian, D.L., 1996. Dynamics of coupled diffusive and decompressive
1271 bubble growth in magmatic systems. *J Geophys Res-Sol Ea*, 101(B8): 17447-17455.
1272 <https://doi.org/10.1029/96JB01342>
1273 Ristić, M.M. and Milosević, S., 2006. Frenkel's theory of sintering. *Science of Sintering*, 38(1): 7-11.
1274 10.2298/SOS0601007R
1275 Russell, A.J., Duller, R. and Mountney, N.P., 2010. 11 Volcanogenic Jökulhlaups (Glacier Outburst
1276 Floods) from Mýrdalsjökull: Impacts on Proglacial Environments. In: J.K. Anders Schomacker
1277 and H.K. Kurt (Editors), *Developments in Quaternary Science*. Elsevier, pp. 181-207.
1278 10.1016/s1571-0866(09)01311-6
1279 Rust, A.C., Cashman, K.V. and Wallace, P.J., 2004. Magma degassing buffered by vapor flow through
1280 brecciated conduit margins. *Geology*, 32(4): 349-352. 10.1130/g20388.2
1281 Saubin, E., Tuffen, H., Gurioli, L., Owen, J., Castro, J.M., Berlo, K., McGowan, E., Schipper, C.I. and
1282 Wehbe, K., 2016. Conduit dynamics in transitional rhyolitic activity recorded by tuffsite vein
1283 textures from the 2008-2009 Chaitén eruption. *Frontiers in Earth Science*, 4.
1284 10.3389/feart.2016.00059
1285 Schipper, C.I., Castro, J.M., Tuffen, H., James, M.R. and How, P., 2013. Shallow vent architecture
1286 during hybrid explosive–effusive activity at Cordón Caulle (Chile, 2011–12): Evidence from

1287 direct observations and pyroclast textures. *Journal of Volcanology and Geothermal*
1288 *Research*, 262(0): 25-37. <http://dx.doi.org/10.1016/j.jvolgeores.2013.06.005>

1289 Shea, T., Hellebrand, E., Gurioli, L. and Tuffen, H., 2014. Conduit- to Localized-scale Degassing during
1290 Plinian Eruptions: Insights from Major Element and Volatile (Cl and H₂O) Analyses within
1291 Vesuvius ad 79 Pumice. *Journal of Petrology*, 55(2): 315-344. 10.1093/ptrology/egt069

1292 Smithsonian, 2016. Katla. <http://volcano.si.edu/volcano.cfm?vn=372030> [04/04/16]

1293 Sparks, R.S.J., 1978. The Dynamics of Bubble Formation and Growth in Magmas - Review and
1294 Analysis. *Journal of Volcanology and Geothermal Research*, 3(1-2): 1-37.
1295 [https://doi.org/10.1016/0377-0273\(78\)90002-1](https://doi.org/10.1016/0377-0273(78)90002-1)

1296 Sparks, R.S.J., 1997. Causes and consequences of pressurisation in lava dome eruptions. *Earth*
1297 *Planet. Sci. Lett.*, 150: 177-189. [https://doi.org/10.1016/S0012-821X\(97\)00109-X](https://doi.org/10.1016/S0012-821X(97)00109-X)

1298 Stasiuk, M.V., Barclay, J., Carroll, M.R., Jaupart, C., Ratte, J.C., Sparks, R.S.J. and Tait, S.R., 1996.
1299 Degassing during magma ascent in the Mule Creek vent (USA). *Bulletin of Volcanology*, 58(2-
1300 3): 117-130. <https://doi.org/10.1007/s004450050130>

1301 Stolper, E., 1982. Water in silicate-glasses: An infrared spectroscopic study. *Contrib Mineral Petr*,
1302 81(1): 1-17. <https://doi.org/10.1007/BF00371154>

1303 Sturkell, E., Einarsson, P., Sigmundsson, F., Hooper, A., Ófeigsson, B.G., Geirsson, H. and Ólafsson, H.,
1304 2010. 2 Katla and Eyjafjallajökull Volcanoes. In: J.K. Anders Schomacker and H.K. Kurt
1305 (Editors), *Developments in Quaternary Science*. Elsevier, pp. 5-21. 10.1016/s1571-
1306 0866(09)01302-5

1307 Sumner, J.M., Blake, S., Matela, R.J. and Wolff, J.A., 2005. Spatter. *Journal of Volcanology and*
1308 *Geothermal Research*, 142(1-2): 49-65. <http://doi.org/10.1016/j.jvolgeores.2004.10.013>

1309 Taniguchi, H., 1988. Surface tension of melts in the system CaMgSi₂O₆-CaAl₂Si₂O₈ and its structural
1310 significance. *Contrib Mineral Petr*, 100(4): 484-489. 10.1007/bf00371377

1311 Tómasson, H., 1996. The jökulhlaup from Katla in 1918. *Annals of Glaciology*, 22: 249-254.
1312 10.1017/S0260305500015494

1313 Tuffen, H. and Castro, J.M., 2009. The emplacement of an obsidian dyke through thin ice:
1314 Hrafninnuhryggur, Krafla Iceland. *Journal of Volcanology and Geothermal Research*, 185(4):
1315 352-366. 10.1016/j.jvolgeores.2008.10.021

1316 Tuffen, H. and Dingwell, D.B., 2005. Fault textures in volcanic conduits: Evidence for seismic trigger
1317 mechanisms during silicic eruptions. *Bull. Volcanol.*, 67: 370-387.
1318 <https://doi.org/10.1007/s00445-004-0383-5>

1319 Tuffen, H., Dingwell, D.B. and Pinkerton, H., 2003. Repeated fracture and healing of silicic magma
1320 generate flow banding and earthquakes? *Geology*, 31: 1089-1092.
1321 <https://doi.org/10.1130/G19777.1>

1322 Tuffen, H., Owen, J. and Denton, J., 2010. Magma degassing during subglacial eruptions and its use
1323 to reconstruct palaeo-ice thicknesses. *Earth-Science Reviews*, 99(1-2): 1-18.
1324 10.1016/j.earscirev.2010.01.001

1325 Uhlmann, D., Klein, L., Onorato, P. and Hopper, R., 1975. The formation of lunar breccias-Sintering
1326 and crystallization kinetics, *Lunar and Planetary Science Conference Proceedings*, pp. 693-
1327 705.

1328 Vasseur, J., Wadsworth, F.B., Lavallée, Y., Hess, K.-U. and Dingwell, D.B., 2013. Volcanic sintering:
1329 Timescales of viscous densification and strength recovery. *Geophys Res Lett*, 40(21): 5658-
1330 5664. 10.1002/2013GL058105

1331 Vergnolle, S. and Jaupart, C., 1986. Separated two-phase flow and basaltic eruptions. *Journal of*
1332 *Geophysical Research: Solid Earth*, 91(B12): 12842-12860. 10.1029/JB091iB12p12842

1333 Villemant, B. and Boudon, G., 1998. Transition from dome-forming to plinian eruptive styles
1334 controlled by H₂O and Cl degassing. *Nature*, 392(6671): 65-69. 10.1038/32144

1335 Villemant, B. and Boudon, G., 1999. H₂O and halogen (F, Cl, Br) behaviour during shallow magma
1336 degassing processes. *Earth and Planetary Science Letters*, 168(3-4): 271-286. 10.1016/s0012-
1337 821x(99)00058-8

1338 Villemant, B., Boudon, G., Nougrigat, S., Poteaux, S. and Michel, A., 2003. Water and halogens in
1339 volcanic clasts: tracers of degassing processes during Plinian and dome-building eruptions.
1340 In: C. Oppenheimer, D.M. Pyle and J. Barclay (Editors), *Geol Soc Spec Publ. Geological Society*
1341 London, Special Publications, Volume 213, pp. 63-79. 10.1144/gsl.sp.2003.213.01.05
1342 Villemant, B., Mouatt, J. and Michel, A., 2008. Andesitic magma degassing investigated through H₂O
1343 vapour-melt partitioning of halogens at Soufriere Hills Volcano, Montserrat (Lesser Antilles).
1344 *Earth and Planetary Science Letters*, 269(1-2): 212-229. DOI 10.1016/j.epsl.2008.02.014
1345 Vosteen, H.-D. and Schellschmidt, R., 2003. Influence of temperature on thermal conductivity,
1346 thermal capacity and thermal diffusivity for different types of rock. *Physics and Chemistry of*
1347 *the Earth, Parts A/B/C*, 28(9-11): 499-509. [http://doi.org/10.1016/S1474-7065\(03\)00069-X](http://doi.org/10.1016/S1474-7065(03)00069-X)
1348 Walker, D. and Mullins, O., 1981. Surface tension of natural silicate melts from 1,200°–1,500° C and
1349 implications for melt structure. *Contrib Mineral Petr*, 76(4): 455-462. 10.1007/bf00371487
1350 Webb, C., Tuffen, H., Owen, J., Castro, J., Berlo, K., Schipper, C.I. and Wehbe, K., 2017. Mid-loaf crisis:
1351 internal breadcrust surfaces in rhyolitic bombs from Chaitén, IAVCEI 2017 Scientific
1352 Assembly, Portland, Oregon, U.S.A.
1353 Westrich, H.R. and Eichelberger, J.C., 1994. Gas transport and bubble collapse in rhyolitic magma: an
1354 experimental approach. *Bulletin of Volcanology*, 56(6-7): 447-458.
1355 <https://doi.org/10.1007/BF00302826>
1356 Whittington, A.G., Hofmeister, A.M. and Nabelek, P.I., 2009. Temperature-dependent thermal
1357 diffusivity of the Earth's crust and implications for magmatism. *Nature*, 458(7236): 319-321.
1358 10.1038/nature07818
1359 Wilson, L., 1980. Relationships between pressure, volatile content and ejecta velocity in three types
1360 of volcanic explosion. *Journal of Volcanology and Geothermal Research*, 8(2-4): 297-313.
1361 10.1016/0377-0273(80)90110-9
1362 Wilson, L. and Head, J.W., 2002. Heat transfer and melting in subglacial basaltic volcanic eruptions:
1363 implications for volcanic deposit morphology and meltwater volumes. *Geological Society,*
1364 London, Special Publications, 202(1): 5-26. 10.1144/gsl.sp.2002.202.01.02
1365 Wilson, L. and Mouginiis-Mark, P.J., 2003. Phreatomagmatic explosive origin of Hrad Vallis, Mars.
1366 *Journal of Geophysical Research: Planets*, 108(E8): n/a-n/a. 10.1029/2002JE001927
1367 Woodcock, D.C., Gilbert, J.S. and Lane, S.J., 2015. Ice-melt rates by steam condensation during
1368 explosive subglacial eruptions. *Journal of Geophysical Research: Solid Earth*, 120(2): 864-878.
1369 10.1002/2014JB011619
1370 Woodcock, D.C., Lane, S.J. and Gilbert, J.S., 2014. Ice-melt rates in liquid-filled cavities during
1371 explosive subglacial eruptions. *Journal of Geophysical Research: Solid Earth*, 119(3): 1803-
1372 1817. 10.1002/2013JB010617
1373 Woodcock, D.C., Lane, S.J. and Gilbert, J.S., 2016. Ice-melt rates during volcanic eruptions within
1374 water-drained, low-pressure subglacial cavities. *Journal of Geophysical Research: Solid Earth*,
1375 121(2): 648-662. 10.1002/2015JB012036
1376 Yokoyama, T., Okumura, S. and Nakashima, S., 2008. Hydration of rhyolitic glass during weathering
1377 as characterized by IR microspectroscopy. *Geochimica et Cosmochimica Acta*, 72(1): 117-
1378 125. 10.1016/j.gca.2007.10.018
1379 Zhang, Y. and Stolper, E.M., 1991. Water diffusion in a basaltic melt. *Nature*, 351(6324): 306-309.
1380 10.1038/351306a0
1381 Zimanowski, B., Fröhlich, G. and Lorenz, V., 1991. Quantitative experiments on phreatomagmatic
1382 explosions. *Journal of Volcanology and Geothermal Research*, 48(3-4): 341-358.
1383 10.1016/0377-0273(91)90050-a